Cardiac Shunts: ASD, VSD, PDA

13

Farhood Saremi

Atrial septum defects (ASDs), ventricular septum defects (VSDs), and patent ductus arteriosus (PDA) are common congenital heart defects in both children and adults [1–3]. Morphological classification of these anomalies is important for treatment decisions. Accurate morphological classification requires imaging technique that is able to identify the defect and define its site, size, and relationship to the structures forming its margins. Imaging technique should also be able to identify associated anomalies, the amount of shunt through the defect, and accurate analysis of the heart and valve functions. Echocardiography is a great method for diagnosis of intracardiac shunts with good resolution to image cardiac morphology in detail and can identify small intracardiac defects and measure the shunt volume. Cardiac MR provides a comprehensive assessment of intracardiac anatomy and accurately quantifies biventricular function and blood flow. Detections of small defects (i.e., apical VSD) may require high-resolution imaging and CT can be the preferred technique. Assessment of associated extracardiac anomalies such as anomalous venous return can be optimally done with CT. In this chapter, a complete review of the shunts and clinical applications of CT and MRI will be presented.

F. Saremi, MD
Department of Radiology, Cardiothoracic Section, University of Southern California, USC Keck Hospital, 1500 San Pablo St., Los Angeles, CA 90033, USA
e-mail: fsaremi@usc.edu

Interatrial Communications

Interatrial communications or ASDs present as an isolated abnormality or in association with other cardiovascular malformations. Generally, ASDs can be categorized into three major types including ostium secundum, ostium primum, and sinus venosus defects (Fig. 13.1). Unroofed coronary sinus (CS) can also be classified in this group although the abnormal defect is not directly related to the interatrial septum. Secundum ASD is the most common type and about two-thirds are seen in females. The exact cause is not clear and genetic factors may play a role. For example, ASD is the most common cardiac malformation of Holt-Oram syndrome and ostium primum defects are seen in 40 % of Down syndrome and may be associated with Ellis-Van Creveld and DiGeorge syndromes [1].

Developmental Considerations and Anatomy

In order to understand anatomy and different anomalies of the interatrial septum, it is necessary to be familiar with certain aspects of the atrial septation and the development of the sinus venosus and the pulmonary vein.

Embryology

Around the fourth week of development, the sinus venosus opens into the posteroinferior part of the common atrium in the midline and receives

F. Saremi (ed.), *Cardiac CT and MR for Adult Congenital Heart Disease*,
DOI 10.1007/978-1-4614-8875-0_13, © Springer Science+Business Media New York 2014

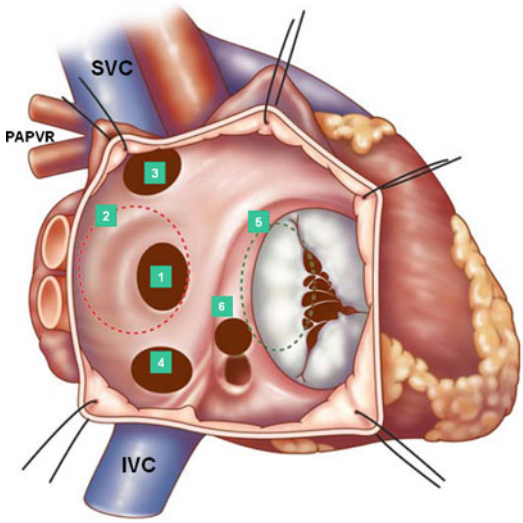

Fig. 13.1 Classifications of atrial septal defect (ASD): (*1*) secundum type 1, (*2*) secundum type 2 (*red circle*), (*3*) sinus venosus (superior), (*4*) sinus venosus (inferior), (*5*) atrioventricular septal (septum primum) defect (*green circle*), and (*6*) unroofed coronary sinus. *PAPVR* partial anomalous pulmonary venous return, *SVC* superior vena cava, *IVC* inferior vena cava

on each side the systemic (common cardinal veins), placental (umbilical), and vitelline (omphalomesenteric) blood by separate paired veins [4–6] (Fig. 13.2). At 5 weeks, the opening of the sinus venosus shifts into the right atrium (sinoatrial orifice) and is guarded by right and left venous valves which unite at the cephalic end of the orifice to form the septum spurium. The pulmonary vein enters the heart as a single structure (common pulmonary vein) with its orifice adjacent to the developing left atrioventricular (AV) junction.

The septum primum is also identifiable medial to the left venous valve and just to the right of the orifice of the common pulmonary vein. At 6 weeks, the liver has invaded the omphalomesenteric and umbilical veins, the umbilical veins have lost their connection with the sinus venosus, and the ductus venosus and intrahepatic portion of the inferior vena cava (IVC) are formed. With these changes, the sinus venosus now receives the two common cardinal veins and the IVC, formed by the termination of

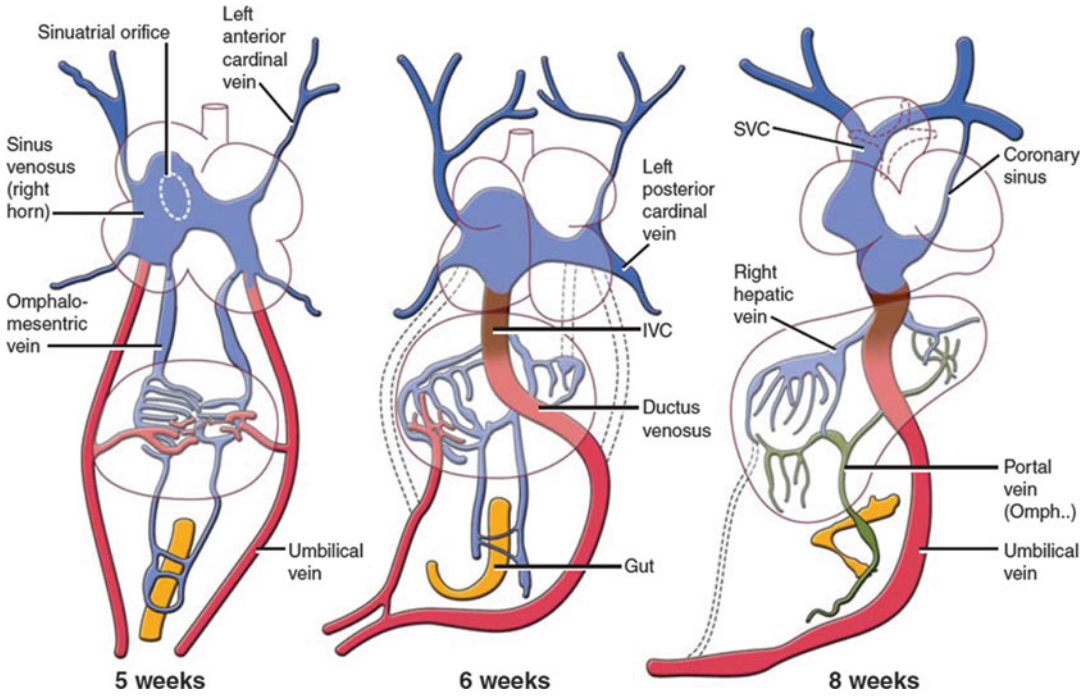

Fig. 13.2 Development of the sinus venosus and omphalomesenteric system. The timing of developments and the relative relationship between structures in cartoons are speculative. *IVC* inferior vena cava, *SVC* superior vena cava

the right omphalomesenteric vein (Fig. 13.2). These connections result in more enlargement of the right horn of sinus venosus. At this time, the septum primum has begun its growth from the roof of the atrial component, carrying on its leading edge a prominent mesenchymal cap. With time, the mesenchymal cap fuses with the atrioventricular cushions, dividing the AV canal into the prospective tricuspid and mitral valve orifices. The dorsal area of fusion grows into the heart tissue and vestibular spine develops which as it fuses with the primary atrial septum ensures that the pulmonary vein enters the cavity of the left atrium. Soon, the upper margin of the septum primum breaks to form a large secondary interatrial communication (ostium secundum or foramen ovale). In the seventh week, the septum secundum starts to form on the right side of the septum primum but the foramen ovale is still large. The septum secundum is nothing but infolding of the roof between the two atria (interatrial groove). The left common cardinal vein and the left horn of the sinus venosus regress, the latter forming the coronary sinus (CS). The superior vena cava (SVC), IVC, and CS now open into the posterior right atrium and find their final location, the so-called sinus venarum (Fig. 13.2). At 8 weeks, the "septum secundum" develops further. The interatrial groove deepens superiorly to separate the opening of the SVC to the right atrium and the attachments of the right pulmonary veins to the left atrium. The interatrial groove is filled by varying amount of extracardiac adipose tissue and is not a true septum. Its thickness determines the prominence of the fossa ovalis margin at its anterosuperior border. In general at 8 weeks, the incorporation of the sinus venosus into the right atrium and separation of the two atria are complete, and the common pulmonary vein has been taken into the left atrium.

By the ninth week, the left sinus valve disappeared. The residual of the septum spurium can be seen as a prominent trabeculation in right atrial appendage near the superior cavoatrial junction. Remnant of the left sinus valve may be seen on the right side of septum secundum on CT or echocardiography studies. The right venous valve will remain as the Eustachian and Thebesian valves guarding the ostia of the IVC and coronary sinus, respectively. By the 11th week, the right and left pulmonary veins have been taken into the left atrium which then contains four pulmonary orifices. As a reminder, the four pulmonary venous components, with separate orifices on both sides of the left atrial roof, do not achieve their definitive positions until after completion of atrial septation. In other words, the "septum secundum" is only seen at the stage when four pulmonary venous orifices are present.

Arial Septum

The normal atrial septum is made up of the floor and rims of the fossa ovalis, with the superior and posterior rims being infoldings of the atrial walls between the attachments of the caval veins to the right atrium and the ostia of the right pulmonary veins to the left atrium [7] (Fig. 13.3).

The floor of the fossa ovalis is formed by the septum primum. It is a relatively thin fibromuscular flap that, anterosuperiorly, overlaps an extensive muscular border, also known as "limbus" which is mainly formed by the septum secundum. In at least 70 %, the flap of fossa ovalis is adhered to the limbus. The inferoposterior border of the fossa ovalis continues directly into the wall of the IVC and its anteroinferior border is continuous with the epicardial fat squeezed between the atria and the ventricles at the AV junction (AV sandwich) (Fig. 13.3). The size of fossa ovalis and its margins may vary greatly. If the seal is incomplete, a patent foramen ovale (PFO) will remain at the anterosuperior quadrant of the rim orientated in a craniocaudal, dorsoventral, and right-to-left axis (Figs. 13.3 and 13.4). A PFO has been known to be a very common finding since 1930, when Thompson and Evans identified a "pencil-patent" defect (0.6–1.0 cm in diameter) within the atrial septum in 6 % of unselected autopsies and a "probe-patent" foramen (0.2–0.5 cm) in 29 % [8]. Hagen et al. found a PFO in 27 % of 965 autopsied hearts [9]. The incidence and size of PFO did not differ with gender but varied significantly with age; 34 % of PFOs occurred in the first three decades, 25 % in the fourth to eighth decades, and 20 % in the

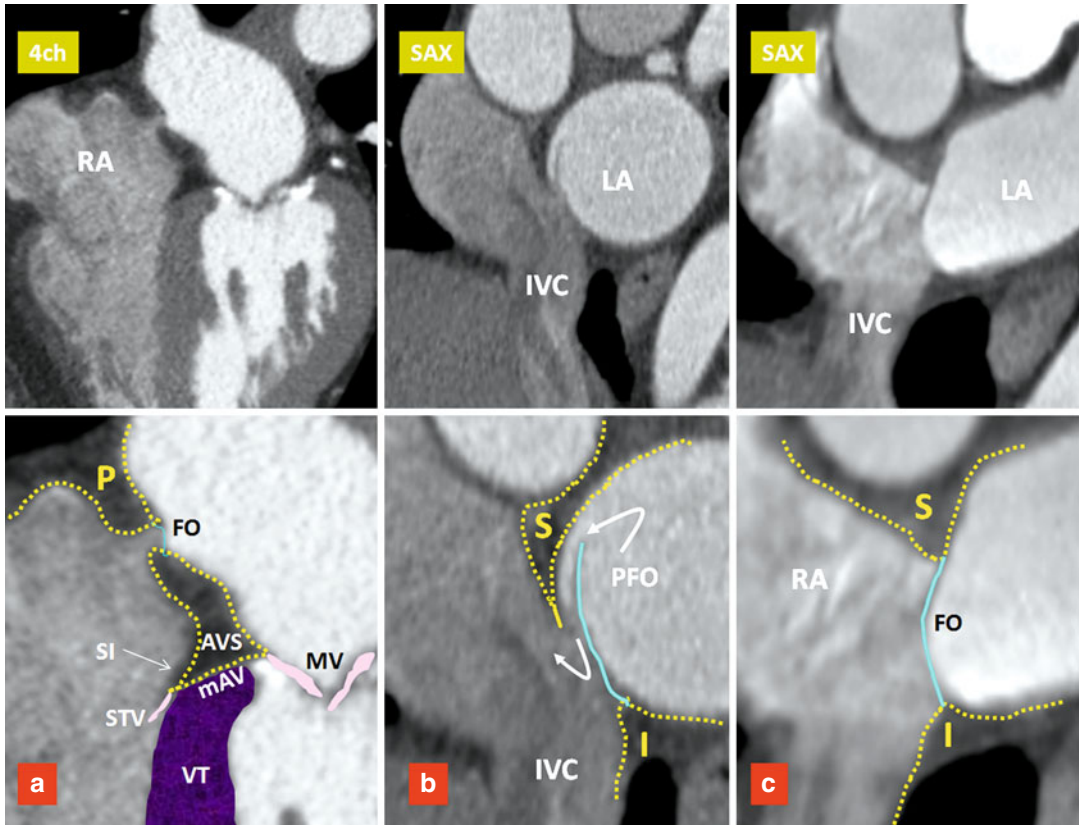

Fig. 13.3 Components of the interatrial septum. Upper row images are four-chamber (*4ch*) and short axis (*SAX*) images of three different patients. Lower row images include magnified views of the upper row images. The septum secundum forms the interatrial groove covering the superior (*S*), posterior (*P*), and inferior (*I*) margins of the fossa ovalis (*FO*). *Blue line* denotes the septum primum. (**a**) Small FO with fatty infiltration of the interatrial groove and atrioventricular sandwich (*AVS*). (**b**) Shows a patent foramen ovale (*PFO*). (**c**) Shows a large FO and a short interatrial groove. *IVC* inferior vena cava, *LA* left atrium, *mAV* muscular AV septum, *MV* mitral valve, *RA* right atrium, *SI* septal isthmus, *STV* septal leaflet of tricuspid valve, *VT* ventricular septum

ninth and tenth decades. The size of the PFO ranged from 1 to 19 mm (4.9 mm, mean) and increased progressively in size from a mean of 3.4 mm in the first decade to 5.8 mm in the tenth decade (perhaps because smaller defects seal with age).

Patent Foramen Ovale

PFO is probably the most common cause of right-to-left shunting in patients with paradoxical embolism [10, 11]. It is also an important mechanism by which an embolic stroke can develop in young patients and appears to be more common in larger PFOs [11]. The presence of shunting through the PFO not only depends upon the transatrial pressure gradient but also likely relates to anatomic features of the PFO; these include the size of opening into the right atrium, length of the PFO tunnel, and the extent of excursion of the flap membrane [11–14]. Moreover, the risk of stroke appears to be increased in the presence of structures that direct flow toward a PFO (i.e., prominent Eustachian valve) or hemodynamic changes that increase right-sided pressure (i.e., large pulmonary embolism). In a study performed by Natanzon and Goldman [14], the magnitude of right-to-left shunting was larger and the length of flap valve was shorter in patients with cryptogenic strokes as compared to those patients whose PFO was

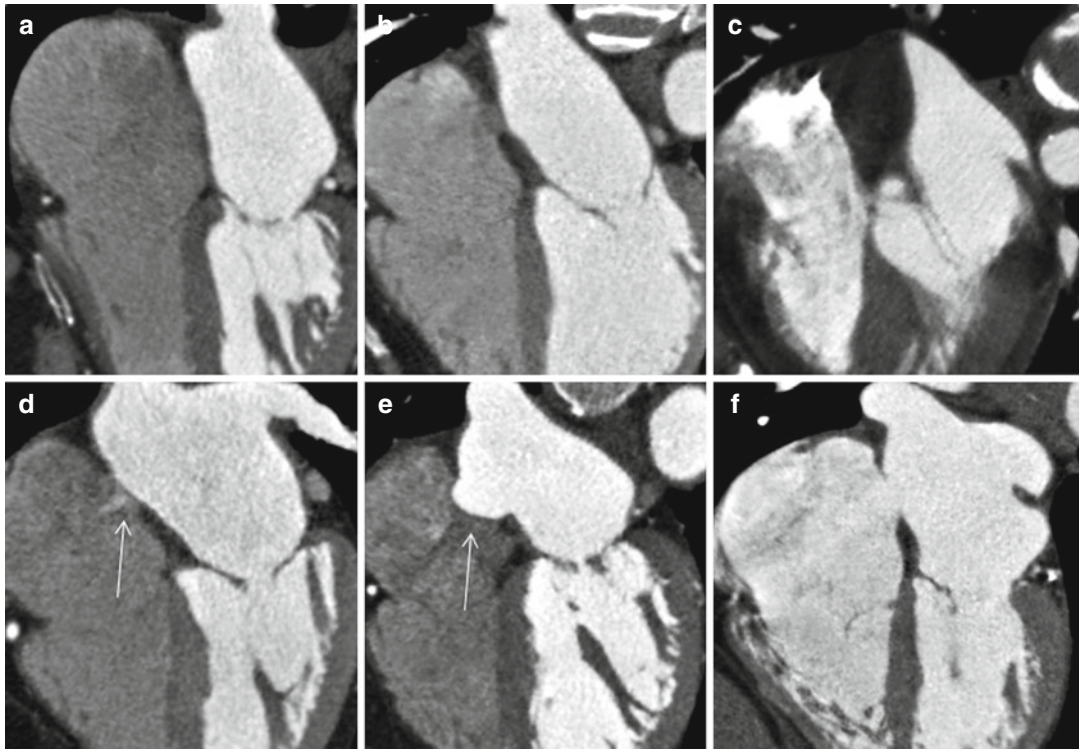

Fig. 13.4 Anatomic variations of the interatrial septum. (**a**) Straight thin line of septum is seen. No appreciable fat is seen in the interatrial groove. (**b**) Thickened interatrial groove due to fat accumulation. Fossa ovalis is well demarcated. (**c**) Severe fatty infiltration of the septum. Fossa ovalis is not seen. (**d**) Small PFO shunt is shown by *arrow*. (**e**) Aneurysm of the atrial septum (*arrow*). (**f**) Secundum ASD

incidentally found on transesophageal echocardiography (TEE). Similar findings have been reported with cardiac CT. In a recent multidetector CT (MDCT) study of asymptomatic individuals, 92 % of left-to-right shunts occurred with a PFO tunnel length of 6 mm or less in length [12]. When the flap length is very short, a bidirectional shunt is more probable. Patients with an atrial septal aneurysm (ASA) also have a very short PFO tunnel length. In a recent postmortem study by Ho et al. [13], two types of PFO were described: valve competent and valve incompetent. PFOs with a short, overlapping flap and with an ASA were classified as incompetent with high likelihood of bidirectional flow. Similar morphology has also been described using MDCT in patients with a short PFO tunnel length or those with an atrial septal aneurysm (ASA) [12] (Fig. 13.5).

Imaging Modalities in PFO Shunt

Imaging diagnosis of a shunt can be performed directly or indirectly. Direct assessment of an intracardiac shunt is mainly performed by echocardiography and MRI; for extracardiac shunts, CT or MR is commonly performed. Given its wide availability, noninvasive nature, and low cost, echocardiography is currently the most popular. With widespread use of cardiac CT for other indications, it has recently gained momentum for the analysis of intracardiac shunts and PFO. MRI enables direct flow quantification and provides valuable information about size, shape, location, and spatial relationship to other structures [15]. However, the present MRI technique may be inferior to contrast-enhanced TEE in detection of right-to-left PFO shunting (i.e., during Valsalva maneuver) and identification of ASA [15–17].

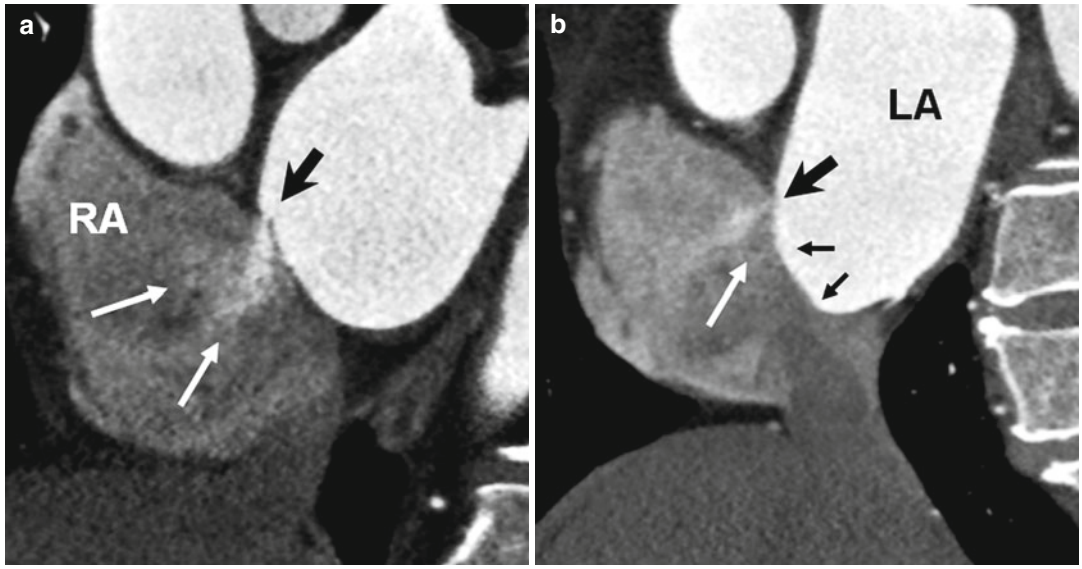

Fig. 13.5 Short axis images show incompetent valves in patent foramen ovale (PFO) with free flow of contrast through the opening (*white arrows*). (**a**) The free flap valve is too short to cover the superior rim of the septum secundum (*black arrow*). (**b**) Atrial septal aneurysm (*small arrows*) also demonstrates very short PFO tunnel (*large black arrow*) causing a left-to-right shunt (*white arrow*). *LA* left atrium, *RA* right atrium

Although TEE is a great modality to show a right-to-left shunt, most of shunts are positive only after the Valsalva maneuver [18]. Demonstration of a PFO tunnel by MDCT may predict the potential for a shunt. Only a limited number of studies have been performed comparing MDCT to TEE [12, 19]. Current CT techniques for coronary angiography are capable of showing a left-to-right shunt. This can be important as demonstration of a left-to-right shunt, particularly when a short flap valve length or ASA exists, indicates an incompetent valve mechanism with high likelihood of a bidirectional shunt (Fig. 13.5). Furthermore, no provocative test is necessary to demonstrate a left-to-right shunt with MDCT. Current techniques for placement of PFO closure devices rely on fluoroscopic landmarks combined with TEE or intracardiac echocardiography guidance [20]. CT has been used for localization of the fossa ovalis to aid for transseptal catheterization [21]. Given that a PFO is a 3-dimensional (3D) structure with dynamic opening and closing, describing the exact size with one simple dimension is not possible. With CT, scan-detailed 3D information can easily be obtained. CT can accurately demonstrate the relationship of important structures to the PFO including the distance to the aortic root, anomalous coronary artery course, and the location of the coronary sinus ostium. These information may be important before device closure placement [12].

Associated Findings with PFO

Chiari Network

The Chiari network represents coarse or fine fibers in the right atrium, arising from the Eustachian or Thebesian valve and strands within the right atrium connecting these valves with the crista terminalis, right atrial wall, or interatrial septum. It is a remnant of the embryonic right valve of the sinus venosus [22, 23] and should be differentiated from a large Eustachian valve by looking carefully for attachments to other parts of the right atrium. A Chiari network has been reported in 2–4 % of autopsy studies [23, 24] and is generally thought to not be of clinical significance. However, in rare instances, the network may be the site of thrombus

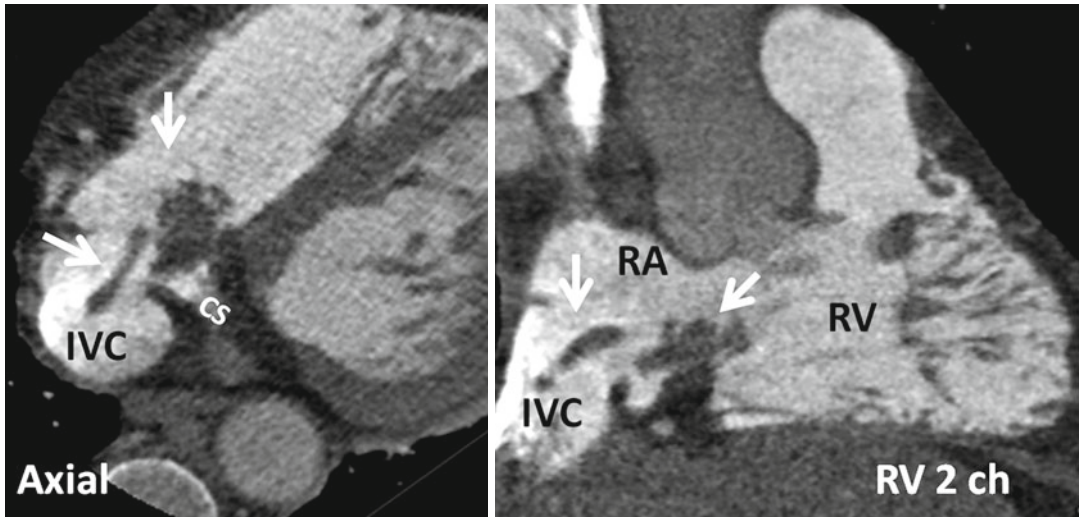

Fig. 13.6 Demonstration of Chiari network with dedicated CT of the right heart. Axial and right ventricle (*RV*) two-chamber (*2ch*) view show rounded and band-like structures (*arrows*) at the inferior cavoatrial junction attaching to the walls of inferior vena cava (*IVC*) and coronary sinus (*CS*) ostia. This was confirmed by echo which also showed possible thrombus covering the network. Patient had a history of right ventricle (*RV*) endocardial pacemaker. *RA* right atrium

formation [25] (Fig. 13.6). In a large study using TEE, a Chiari network was seen in 2 % [26]. Chiari network is frequently associated with a PFO (83 %), right-to-left shunting (55 %), and an ASA (24 %). Fine networks may be difficult to visualize with CT or MRI. With special right heart imaging techniques to clearly opacify the right atrium, a Chiari network may be seen in selected MDCT studies (Fig. 13.6).

Atrial Septal Aneurysm

An ASA is another important anatomic feature to consider in evaluating a PFO. The incidence of ASA is 4.6–10 % [27–29] by TEE. An ASA is associated with a PFO with a prevalence of 30–60 % [30–32] and is most likely associated with an increased rate of embolic events [33]. The prevalence of an ASA in patients with cerebral ischemia and normal carotid arteries is higher (28 %) than in patients without cerebral ischemia (10 %) [29]. An ASA can easily be assessed by CT and MRI. In one study with MDCT, an ASA was seen in 4 % of patients, and 63 % of patients with ASA were found to have a left-to-right shunt [12] (Fig. 13.5). An ASA is defined as a bulging of >15 mm beyond the plane of the atrial septum [34] and classified according to Hanley's diagnostic criteria by Pearson [33] into two types based on the direction and timing of protrusion. Generally, right atrial protrusion is the most common (76 %) and usually shows transient motion toward the left atrium during systole or with the Valsalva maneuver [33] (Fig. 13.7). Increased interatrial septum mobility is believed to enhance the probability of paradoxical embolism by mechanically directing blood flow from the IVC through the PFO into the left atrium.

Persistent Eustachian Valve in Adults

The Eustachian valve (EV), which guards the anterior-inferior aspect of the IVC, is a remnant of the embryonic right valve of the sinus venosus. Embryologically, the EV directs oxygenated blood from the IVC across the PFO into the systemic circulation [35] (Fig. 13.8). By directing the blood from the IVC to the interatrial septum, a persistent EV may prevent spontaneous closure of the PFO after birth and may, therefore, indirectly predispose to paradoxical embolism. A prominent EV is a common finding in CT or MRI studies of the heart and thorax and should not be mistaken with a thrombus.

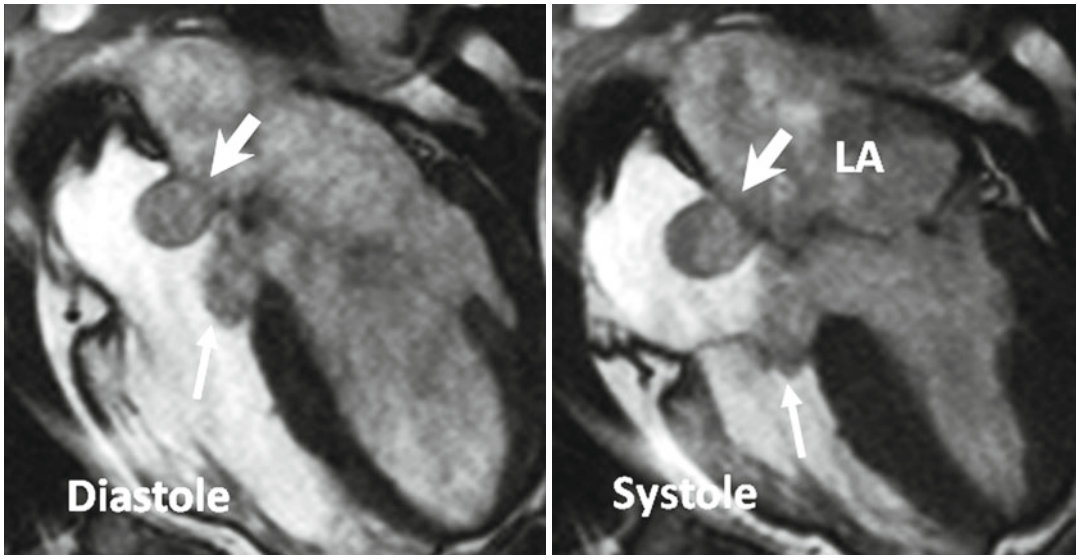

Fig. 13.7 Large atrial septal aneurysm (*thick arrows*) with persistent protrusion into the right atrium during cardiac cycle. A relatively large membranous septum aneurysm also exists (*thin arrows*)

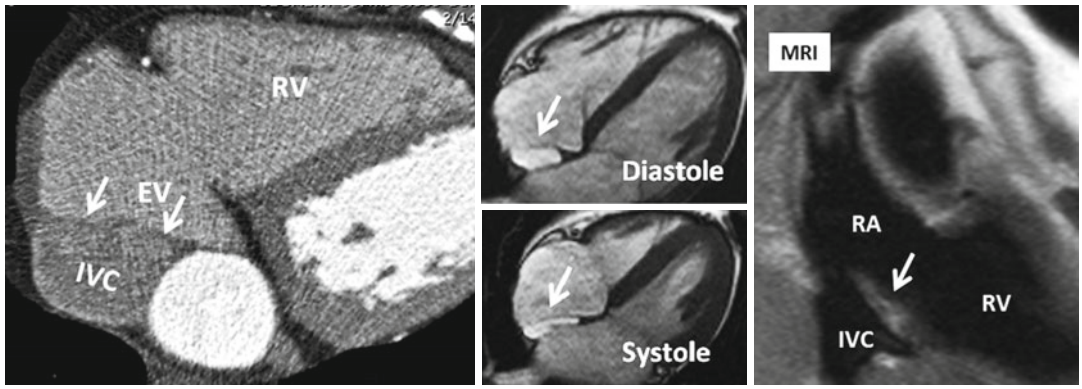

Fig. 13.8 Prominent Eustachian valve (*EV*) shown on axial CT and MR images (*arrows*). The EV guards the anterior-inferior aspect of the inferior vena cava (*IVC*). Note variation in morphology on systolic and diastolic images. *RA* right atrium, *RV* right ventricle

Cardiac MR Techniques

In general, MR protocols for intracardiac shunts contain most of the routine sequences. The choice of sequences and extent of coverage depend on the anatomy of interest. For example, in PDA analysis, MR angiography of the great vessels is necessary and the choice of cine and phase-contrast sequences can be individualized. As an another example, the entire chest is covered when looking for partial anomalous pulmonary venous return (PAPVR). An overview of MR protocol is listed below.

Protocol

Positioning

Scout images will be obtained in supine. Table repositioning will be made to place the anatomy of interest (i.e., interatrial septum) at the magnet isocenter.

Morphological Imaging

Two-dimensional axial, sagittal, and coronal images to define cardiovascular anatomy. Both dark- and bright-blood images are acquired with half-Fourier fast-spin-echo and balanced

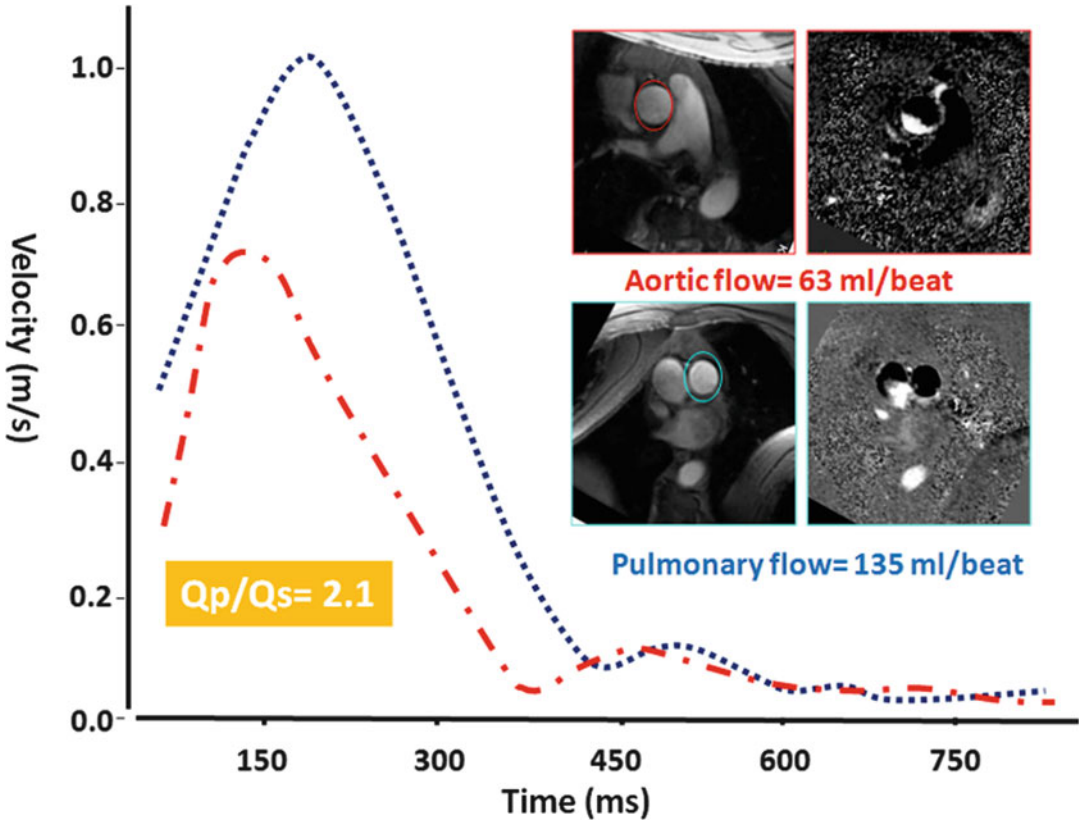

Fig. 13.9 Qp/Qs ratio assessment in a patient with ASD showing 2:1 shunt ratio. Slice position for phase-contrast MRI in the ascending aorta and pulmonary trunk is approximately 2.0 cm above the respected valve

steady-state free-precession (b-SSFP) sequences, respectively. Slice thickness of 6- and 2-mm interslice gap are enough.

Cine Imaging

It is for initial assessment of the intracardiac shunts and analysis of ventricular function. A segmented b-SSFP sequence is used with retrospective ECG gating during repeated 8-s breath holds (slice thickness, 8 mm; no gap). Standard long axis images will be obtained to cover the entire heart from the apex to the atrial base. In our institution, 4-chamber or axial views of the entire heart are obtained in all patients. With a matrix of 256, typical in-plane resolution is 1.7–1.4 mm. Temporal resolution will be 35 ms/phase.

Velocity-Encoded Imaging

Phase-contrast (PC) techniques include direct and indirect assessments of the shunt. Indirect assessment consists of comparing flow in the pulmonary artery (Qp) and aorta (Qs) (Fig. 13.9). Velocity-encoded images are generally acquired using a retrospective vector-ECG gating during repeated expiratory 12–18-s breath holds. Retrospective vector-ECG gating is used in almost all PC MR protocols to include end-diastolic flow. Breath hold technique is preferred to free breathing especially for direct assessment of shunt. For indirect shunt volume measurement, a free-breathing method with multiple measurements (number of excitations = 3–4) can be used to increase precision [36, 37].

Typical parameters are as follows: slice thickness, 5–6 mm; in-plane resolution, 1.5–2 mm; 18–20 reconstructed heart phases (temporal resolution, 25–30 ms/phase); flip angle 25°; and echo time, 2.8–3.0 ms. Velocity-encoding values differ depending on the anatomy and location and size of shunt. General values include 70–100 cm/s for

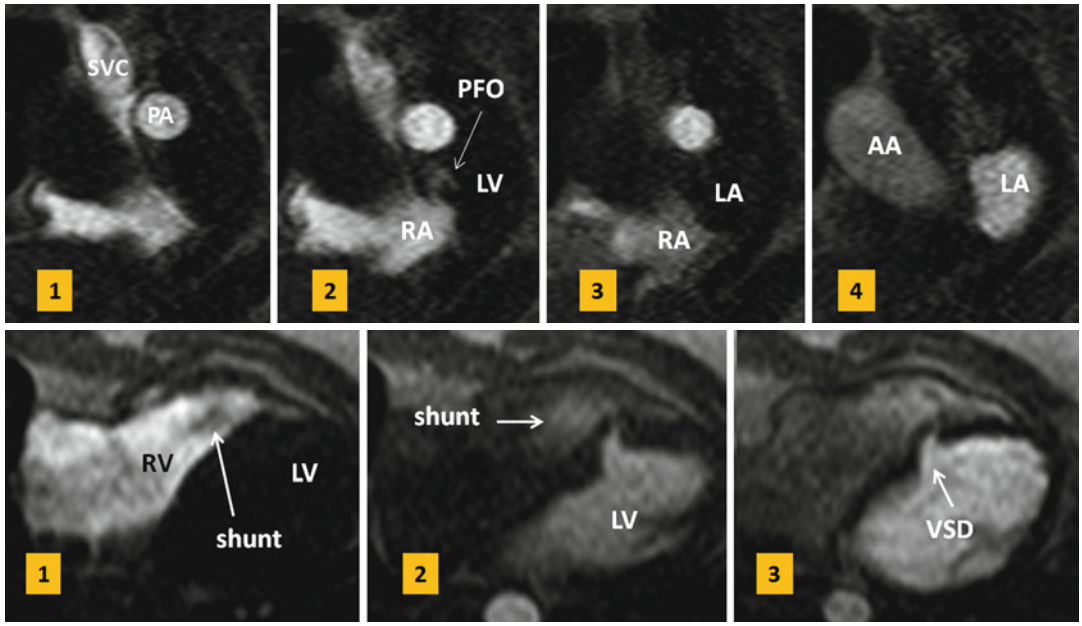

Fig. 13.10 *Upper row*: first-pass MR angiograms in a patient with patent foramen ovale (*PFO*). Short axis series during the Valsalva at atrial level show a small puff of contrast (*arrow*) from right to left at the level of PFO on the third image which disappeared on image 4. *Lower row*: small muscular ventricular septal defect (*VSD*) with left-to-right shunt is shown on first-pass MR angiogram. On the first image, non-enhanced blood is passed into the right ventricle (*RV*). On the second image, contrast-enhanced blood is shunted from the left ventricle (*LV*) into the right through a muscular VSD. *SVC* superior vena cava, *PA* pulmonary artery, *RA* right atrium, *LA* left atrium, *AA* ascending aorta

ASD, 100–200 for VSDs, 100–300 cm/s for PDA, and 150–250 cm/s for arteries.

MR Angiography (MRA)

Three-dimensional gadolinium-enhanced MRA using fast gradient-echo sequence provides further evaluation of any PAPVR. Coronal views are preferred to cover entire heart and major vessels. Alternatively, non-ECG-gated time-resolved MRA can be performed. In case of ASD, 10 mL of gadolinium-based contrast agent followed by a 20-mL saline flush at a flow rate of 5 mL/s will be injected and axial image is obtained. Shunts can be evaluated visually or by analysis of time-intensity curves extracted from measurements within the left atrium, right atrium, and pulmonary vein ostia. This technique has been described for diagnosis of patent foramen ovale during the Valsalva [15]. It can similarly be utilized in selected cases (without or with Valsalva) for diagnosis of other intracardiac shunts. Second alternative is a saturation-recovery gradient-echo sequence commonly used for myocardial perfusion imaging. It will be modified to a non-ECG-gated sequence to acquire continuous data at 6 frames per second during a proper Valsalva maneuver [17] (Fig. 13.10).

Shunt Quantification

MR velocity and flow quantification is mainly performed by PC velocity-encoding (VEC) sequences, which elicit contrast from the phase of a spin's transverse magnetization [38, 39] (Fig. 13.11).

TEE usually allows exact localization and sizing of the shunt defect. However, determination of shunt volumes by Doppler echocardiography has limitations [40]. TEE is semi-invasive and might have limitations in visualization of adjacent structures and anomalous venous return. Invasive oximetry using Fick's principle is the gold standard for the quantification of left-to-right shunting

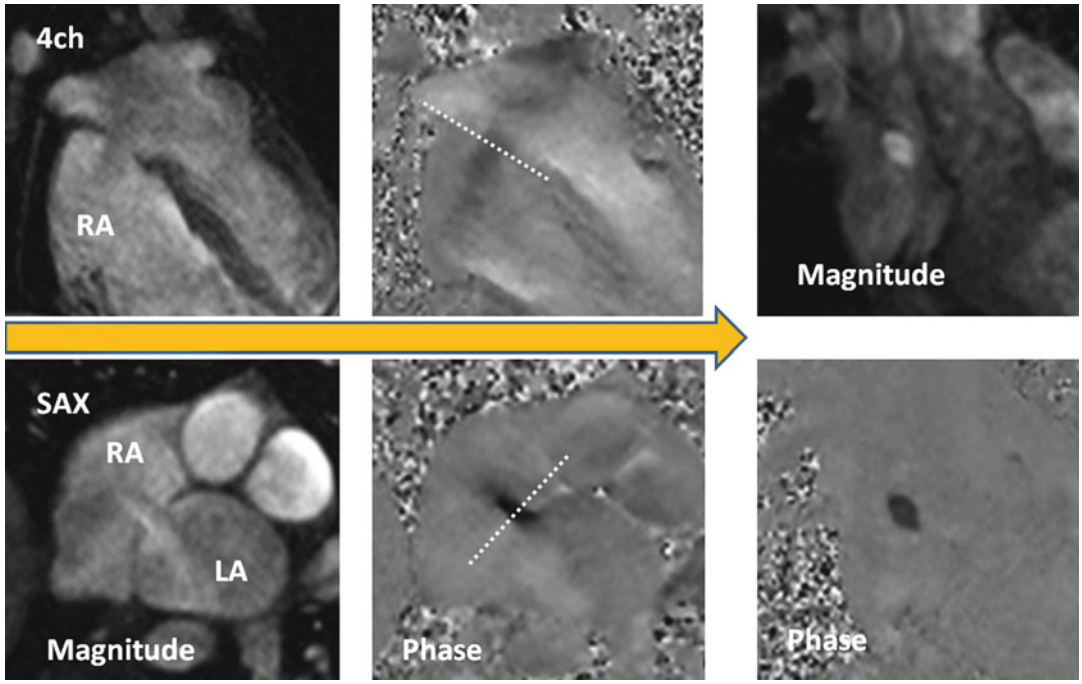

Fig. 13.11 Steps to obtain the optimal imaging plane for en face VEC MR of secundum ASD. It is important to know that the ASD flow direction is not often orthogonal to the plane of the interatrial septum and that the interatrial septum moves during cardiac cycle. To take into account these facts, two orthogonal phase-contrast images along the plane of shunt flow will be obtained. Using these reference planes, final phase-contrast image will be acquired perpendicular to the jet of flow close to the atrial septum and when the shunt flow is maximum. *LA* left atrium, *RA* right atrium

based on measurements of blood oxygenation but is not without limitations [41, 42].

In VEC MR, the phase of flowing protons relative to stationary protons along a magnetic gradient changes in proportion to flow velocity [38]. The change in phase angle is mapped on phase images, and flow velocity is computed with a standard formula. To determine flow volume across a shunt or vessel lumen, the spatial mean velocity of the area of interest is multiplied by the cross section of that area and repeated at each cine frame using automated or semiautomated methods available in most workstations. The region of interest around the blood vessel in each frame may require redrawing for motion and vessel compliance during the cycle. VEC MR imaging flow measurements taken at multiple (usually 16 or 32) evenly spaced points in the cardiac cycle can be plotted against time to construct a flow curve. The area under the curve can be integrated to derive flow volume for a given cardiac cycle.

Technical Considerations

Through-plane flow encoding of the septal defect or a vessel should be assessed in a plane perpendicular to main direction of flow. Underestimation of velocity and flow can result if the target structure is not imaged in a plane perpendicular to flow or if partial volume averaging occurs [43, 44]. Thick slices and volume averaging cause underestimation of flow. The estimation of flow can still be corrected up to 15° deviation from the orthogonal imaging plane. Up to this angle, the increase in vessel area is compensated for by the increase in partial volume effects [43]. Aliasing may occur if the selected velocity-encoding value is lower than the actual peak velocity at any time during the cardiac cycle. Care must be taken not to set the velocity-encoding values too high as this will increase the noise. Noise peaks may interfere with

measurement of the peak velocity; however, the estimation of flow is less affected because the noise is averaged over cross-sectional area of the targeted structure [44, 45]. For small vessels, if the vessel diameter is less than 2–2.5 mm (four to eight pixels), accuracy of flow measurements may suffer [46]. Shimming of the magnet before scanning is necessary to compensate for local field inhomogeneity. Faster acquisition is the key to improve phase-offset errors that can occur between bipolar gradients in PC MR. Single breath hold probably causes less artifacts compared to long free-breathing acquisition that may take of 2–3 min. A recent study has shown higher value for pulmonary flow in breath hold technique compared with free-breathing method [47]. Low cardiac output value is expected in retrospective method compared with prospective technique. Therefore, same method should be used for follow-up examinations. In routine practice, the TE is kept short to minimize the time interval in which these phenomena can develop [48]. For technical reason, there is a limit to our ability to shorten the TE to a certain limit. Correct positioning of the patient is another important factor. It would cause less error when the anatomy of interest (i.e., interatrial septum) is placed as close as possible to the magnet isocenter [17]. Phase-offset errors such as those from nonlinear gradients increase with distance from the isocenter. With technological advances in MR imaging, faster data acquisition in single breath hold is possible. Parallel imaging techniques continue to improve and higher acceleration factor can be used in clinical practice. Unfortunately, parallel imaging accelerates acquisition at the expense of a lower signal-to-noise ratio. Therefore, combination with parallel imaging is only recommended when signal-to-noise ratio is not of critical importance for diagnostic image quality.

Aortic and Pulmonary Flow Quantification

VEC MR is an accurate method to measure the amount of shunt. Left-to-right shunting can be calculated indirectly by measuring flow Qp/Qs ration which is the ratio of right ventricle stroke volume to left ventricle stroke volume. For Qp/Qs ratio, VEC MR is shown to correlate well with echocardiography, invasive oximetry, and radionuclide angiography, although this approach does not provide information about the size, shape, or location of a defect [37, 46, 49–53]. Using VEC MR, a 5 % difference between flow in the ascending aorta and flow in the pulmonary artery in healthy individuals is calculated [49, 54]. Therefore, although Qp/Qs measurement by VEC MR may correlate with true shunt severity, this approach is limited when the shunt volume is small. In this case, direct shunt volume measurement is preferred.

Slice position in the ascending aorta is approximately 2.0–3.0 cm above the aortic valve and distal to the coronary arteries at the level of the right pulmonary artery (Fig. 13.9). Slice position in the pulmonary trunk is approximately 1.5–2.0 cm above the pulmonary valve but proximal to the bifurcation. Placing the imaging plane at level of valve should be avoided due to turbulent flow and valve motion. Some have suggested to place the aortic slice at level of coronary artery ostium to include coronary blood flow [55], although this level of slice selection does not seem to be a good choice as the cross-sectional area of the aorta at sinus of Valsalva especially at the level of left main coronary ostium is larger than the aorta above it and may interfere with correct flow calculations. Flow measurements in the ascending aorta distal to the coronary ostia would miss coronary blood flow. For this technical limitation, some have suggested to use Qp/Qs ratios of >1.75:1 as PC MRI threshold for surgery. In reality, diastolic flow into the coronary arteries is minimal (0.5 % of the cardiac output) [56] and even smaller than the errors expected from the PC technique of measurements to cause additional problem. Left-to-right shunts in ASD and VSD are calculated by the following formula: percentage of left-to-right shunt = (Qp−Qs)/Qp. In PDA, it would be (Qs−Qp)/Qs.

Direct Imaging of the Shunt

VEC MR analysis of the outflow tracts is simple, reliable, and straightforward in execution. In a recent study of 35 adult patients with ASD, VSD, and PDA, PC MRI was referenced to transthoracic echo and found to have 93 % specificity and 100 % sensitivity for description of

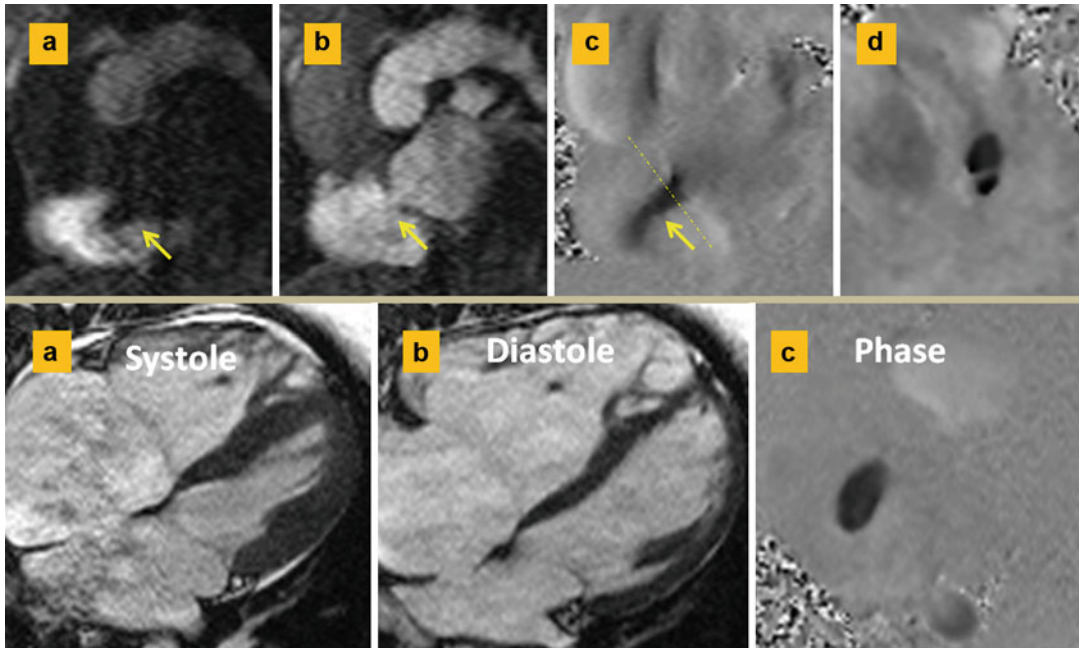

Fig. 13.12 Septum secundum ASD. *Upper row*: (**a** and **b**) are short axis first-pass MR angiographies at the level of ASD. Left-to-right shunt is shown as a negative band in the right atrium in (**a**). This is best confirmed on phase-contrast image (**c**). (**d**) Through-plane phase image shows a double-barrel ASD. *Lower row*: different case shows ASD diameters change with cardiac cycle. The maximum diameter is usually at ventricular systole (**a**) when the atria are largest. Smaller length is seen in diastole (**b**). Typical oval-shaped ASD at the time of maximal flow is shown in the phase image (**c**)

shunts with a Qp:Qs greater than 1.5 [57]. In contrast, direct measurement of shunt flow through the defect requires more experience and precision to get correct results. With direct shunt imaging, flow quantification, as well as size, and morphology analysis are possible which may have incremental clinical value especially for percutaneous closure candidates. The technique of direct en face shunt analysis is described in detail for ASD by Thompson et al. [17] and good correlations with echocardiography in adults were reported. In children, direct flow measurements may be difficult and inaccurate compared with Qp/Qs [37]. This is probably because in children higher heart and respiratory rates, along with higher peak velocities and smaller structures, can lead to increased error on VEC MR [51]. Newer sequences such as 4D phase-contrast sequence can improve visualization of cardiac shunts compared to conventional cardiac MR imaging.

The first step for direct shunt analysis is to review the cine images visually and determine whether flow can be detected (i.e., across the interatrial septum). If shunt is not visible on cine images, still PC images will be obtained at the level of septum to completely rule it out.

Velocity encoding is initially set low (60 cm/s) to ensure sensitivity for lower blood velocities.

Three contiguous through-plane PC slices will be acquired parallel to the septum with the middle cut in the septum. If the shunt is seen, through-plane VEC MR should be obtained perpendicular to the direction of shunt flow rather than simply perpendicular to the morphological plane of the septal defect [17]. To minimize errors, all phases of cine images will be reviewed and the imaging planes are prescribed at the time when the shunt flow is maximal (i.e., end-systole). Defect area is also measured by planimetry when shunt flow is maximal (Fig. 13.12).

Classification of Interatrial Communications

Secundum ASD

Secundum ASD is the most common ASD usually seen in middle-aged women [1]. It may be discovered in routine clinical examinations or imaging study of the heart as it is asymptomatic in 90 % of cases. Symptoms include palpitation, atypical chest pain, or those related to paradoxical embolism. Imaging demonstration of morphological variations in size, position, and shape of secundum ASD is important particularly since the widespread use of transcatheter closure techniques. Secundum ASD can be divided into two types depending on location [58]. Type one is the result of abnormal development of the septum primum [59] and is seen in 85 % of cases [58] (Fig. 13.13). In type one, the limbus is intact. The defect is usually oval shaped with a mean size of 1.8–2.8 cm on MR measurements [17]. The size of defect changes with cardiac cycle (Fig. 13.12). The defect area is usually reduced concentrically [60]. The most common location of defect is central with one or multiple holes (fenestrated) [58, 61]. Other variants include complete absence of the flap valve and an anterosuperior defect. Type two is less common (15 %). This type is characterized by abnormal development of the septum secundum or superior limbus of the fossa ovalis resulting in a superiorly located large ASD and an intact septum primum. The atrial roof without any substantial rim forms the superior border of the defect. This is in contrast to superior sinus venosus defects, in which the interatrial communication is located posterosuperior to the normally developed superior limbus. It seems that the two forms of secundum ASD have different pathogenesis.

Sinus Venosus Defects

Sinus venosus defects are relatively uncommon forms of interatrial communication (<15 %) [62, 63]. These abnormal venoatrial communications produce shunting between the two atria as a result of anomalous pulmonary venous connection to

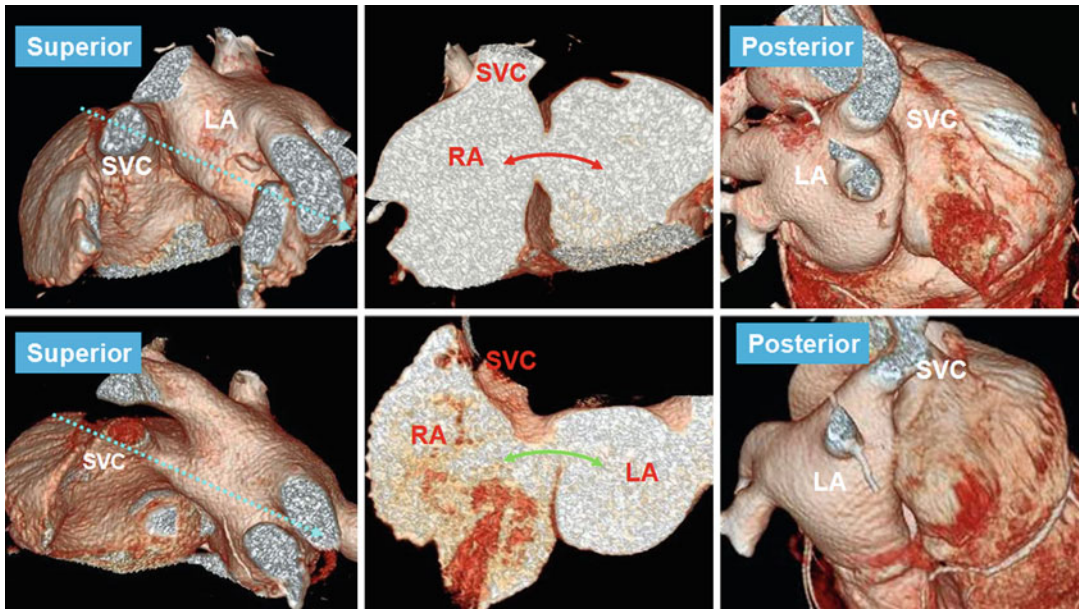

Fig. 13.13 Type 1 (*upper row*) and type 2 (*lower row*) of secundum ASD. Anterosuperior views show incomplete development of the interatrial groove in the superior aspect of the septum in type 2 secundum ASD causing a superiorly located defect (*curved green arrow*) and an intact septum primum compared with type 1 in which the defect is central in the septum primum (*curved red arrow*) but the superior groove is well formed. Note that posterior groove is relatively well developed in both conditions. *Dashed arrows* (*left images*) show the cross-sectional cuts through the ASD shown on the *middle images*

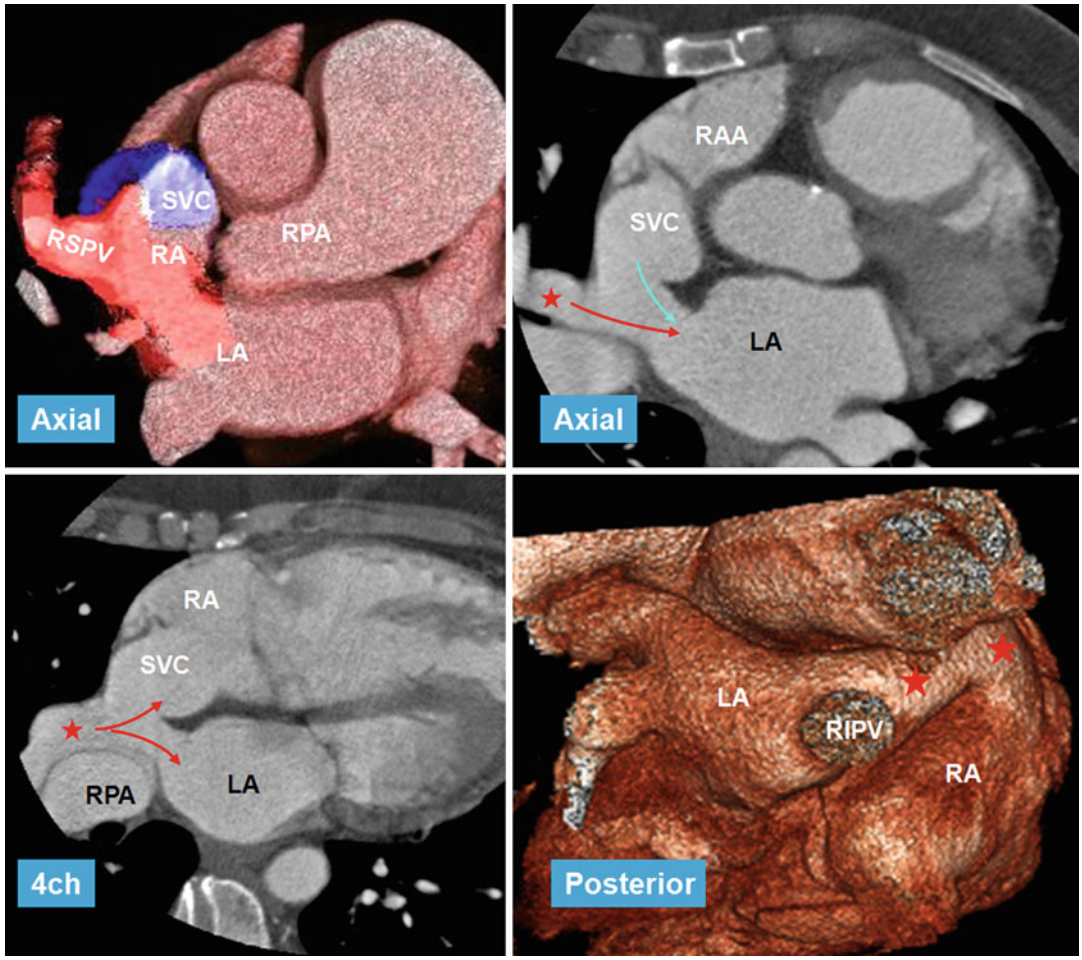

Fig. 13.14 CT images in 56-year-old female referred for evaluation of right heart enlargement and pulmonary hypertension showing sinus venosus defect as a result of anomalous connection of the right superior pulmonary vein (*RSPV*) (*red stars*) to the superior vena cava (*SVC*) while maintaining its connection to the left atrium (*LA*) (venous-venous malformation). Overriding of RSPV above the septal defect is shown on four-chamber view (*4ch*). Pulmonary flow (*red arrows*) and systemic SVC flow (*blue arrow*) can enter both atria. Posterior volume-rendered view shows RSPV bridging (*red stars*) between the two atria. *LA* left atrium, *RA* right atrium, *RIPV* right inferior pulmonary vein, *RPA* right pulmonary vein, *RAA* right atrial appendage

one of the caval veins (venous-venous malformation) while retaining its connection to the left atrium (Fig. 13.14) or an abnormal vena cava with a large hole at its ostium that overrides the intact rim of the fossa ovalis [64–67] (Fig. 13.15). The caval vein can therefore participate in the formation of a large interatrial communication outside the confines of the fossa ovalis. In other words, this anomaly would be correctly defined as an anomalous venoatrial communication rather than representing an interatrial communication.

Two variants are described, superior and inferior. The superior variant is related to the SVC and the inferior variant is in connection with the IVC. The inferior variant is rare and usually diagnosed in children [68]. The crucial anatomic and imaging diagnostic element is the establishment of the integrity of the rims of the oval fossa. Association with PAPVR exists in more than 90 % of cases [69], most commonly involving the right superior pulmonary vein. Involvement of the left pulmonary veins is rare. Abnormal pulmonary venous

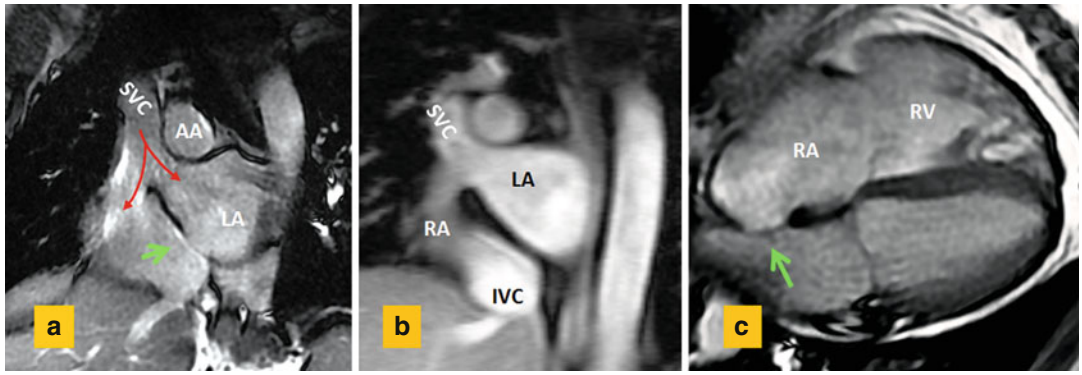

Fig. 13.15 Sinus venosus ASD in 55-year-old male with right heart enlargement. (**a**) Short axis cine view and (**b**) MR angiogram at basal level of the heart show the superior vena cava (*SVC*) riding over the superior septal defect with blood (*red arrows*) flowing into both the right atrium (*RA*) and the left atrium (*LA*). (**c**) Four-chamber view shows dilated RA and right ventricle (*RV*). Intact fossa ovalis is shown by *green arrows*. *AA* ascending aorta, *IVC* inferior vena cava

connections are not a prerequisite for diagnosis and can exist with other types of ASD. It is also possible for the SVC to remain connected to the right atrium only, without any overriding.

Sinus venosus defects may remain asymptomatic until the third or fourth decade of life despite substantial left-to-right shunting [1]. The hemodynamic abnormality is similar to other shuntings between the atria, and it is not possible based on clinical features to differentiate the sinus venosus defect from other forms of interatrial communications [70]. Increased blood flow through the right heart chambers may eventually lead to right ventricular failure. There is threefold greater risk of developing pulmonary arterial hypertension in patients with sinus venosus defects and developing it at younger age than patients with secundum ASD, which highlights the need for correct diagnosis [71].

Accurate demonstration of the abnormal anatomic pathway allows the surgeon either to patch or to baffle the pulmonary and caval pathways to the appropriate atrium without causing obstruction or permitting a residual shunt. Comprehensive imaging diagnosis of sinus venosus defect can be challenging. TEE is superior to the transthoracic approach in adults, with only one-quarter of the defects being correctly diagnosed in transthoracic echocardiography [72]. The majority of diagnostic difficulties arise from the poor acoustic windows. Even with TEE using conventional scan planes, the defect can be missed [73]. Demonstration of PAPVR with TEE is also challenging and in some cases can be frustrating especially for veins that connect to SVC more than 2 cm above the superior cavoatrial junction. Such information is crucial if surgical intervention is being considered. Adult patients with left-to-right shunting and enlarged right heart shown by transthoracic echocardiography should be further evaluated with MRI or CT (Fig. 13.14).

Both CT and MRI are great imaging methods to evaluate these abnormalities particularly for the diagnosis of anomalous pulmonary venous return [74, 75]. It is not uncommon to see a PAPVR with secundum ASD [66]. In an echocardiographic review by al Zaghal [66], 4 of 11 defects initially reported as superior type of sinus venous defect were found to be within the fossa ovalis with abnormal connection of the pulmonary veins to the right atrium in three cases. Therefore, distinction of the septal boundaries is crucial in providing solid criteria for diagnosis. Any problem in formation of superior part of interatrial septum will result in type 2 secundum ASD as described earlier (Fig. 13.13). Communications outside the confines of the true septum can take the form of sinus venosus defects, coronary sinus (CS) defects, and atrioventricular septal defect (AVSD) of "ostium primum" variety [66].

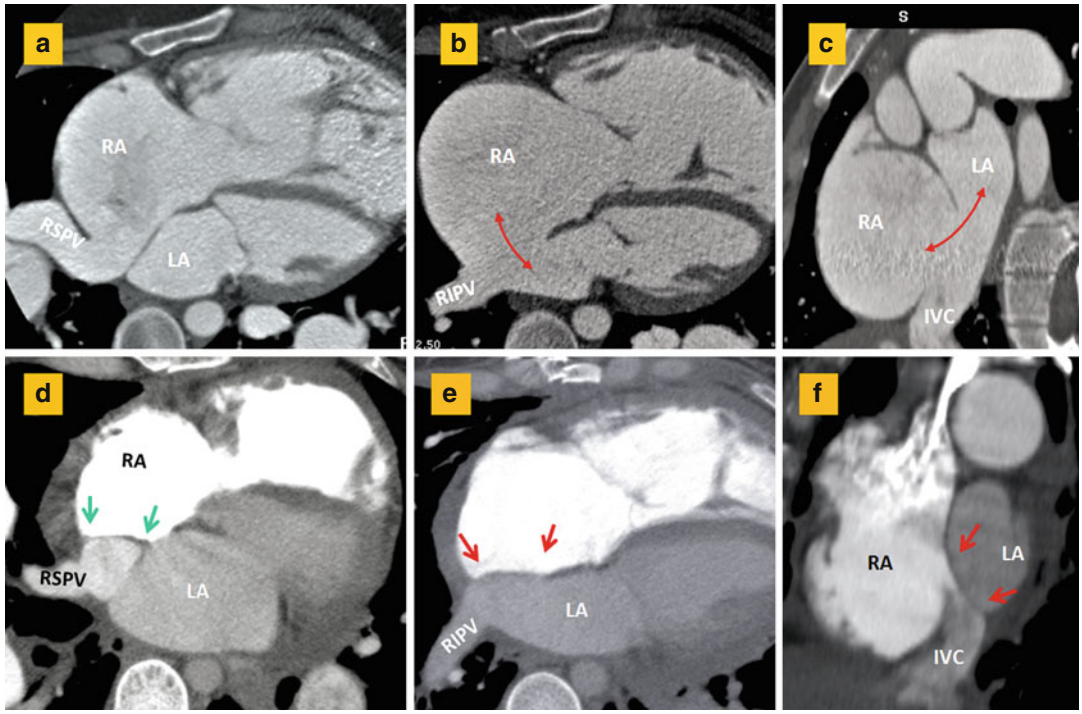

Fig. 13.16 (**a**–**c**) CT images before surgery show anomalous drainage of the right superior pulmonary vein (*RSPV*) into the right atrium (*RA*) in association with a large atrial septal defect (*double-headed arrows*) involving inferior aspect of the interatrial septum. Short axis image (**c**) shows large inferior septal defect and overriding of the inferior vena cava (*IVC*) over both atria making it difficult to differentiate a large secundum defect from an inferior sinus venosus defect. (**d**–**f**) Corresponding after surgery images show closure of the atrial septal defect (*between red arrows*) and baffling of the RSPV flow (*between green arrows*) into the left atrium. The right inferior pulmonary vein (*RIPV*) is normally draining into the left atrium (*LA*)

The diagnosis of inferior variant can be more difficult. Again, it is important to find the fossa ovalis rim intact. The Eustachian valve should not be mistaken with inferior border of the defect.

In contrast to superior variant, PAPVR is uncommon in the inferior sinus venosus defect [76], and overriding of the IVC appears to be the cause (Fig. 13.16). If the pulmonary vein participates in abnormal connection to the IVC, then it should continue its normal course to connect to the left atrium [67]. If the pulmonary vein did not maintain normal connection to the left atrium, the IVC would connect only to the right atrium, resulting in partial return to the IVC (scimitar) or the inferior right atrium.

Atrioventricular Septal Defect

Detailed AVSD is described in Chap. 17. In AVSD, the atria and the ventricles are separated by a common AV valve with one valve ring [77]. This common valve consists of five leaflets: a superior (anterior) bridging leaflet, an inferior (posterior) bridging leaflet, a left mural leaflet, a right mural leaflet, and a right anterolateral leaflet. A constant imaging feature is loss of normal offsetting of atrioventricular valves. Two morphologies are described, complete and partial [77]. Partial form is more common. In a complete AVSD, one single valve orifice exists. In the partial form, the free margins of the bridging leaflets are fused, creating two separate valve orifices sharing a common valve ring. Unlike a normal two leaflet mitral valve, in partial AVSD, the left AV valve (cleft mitral) has three leaflets. An intermediate or transitional AVSD is also described showing two valves with ASD and VSD. In complete AVSD, there is usually an ostium primum ASD and a large VSD between

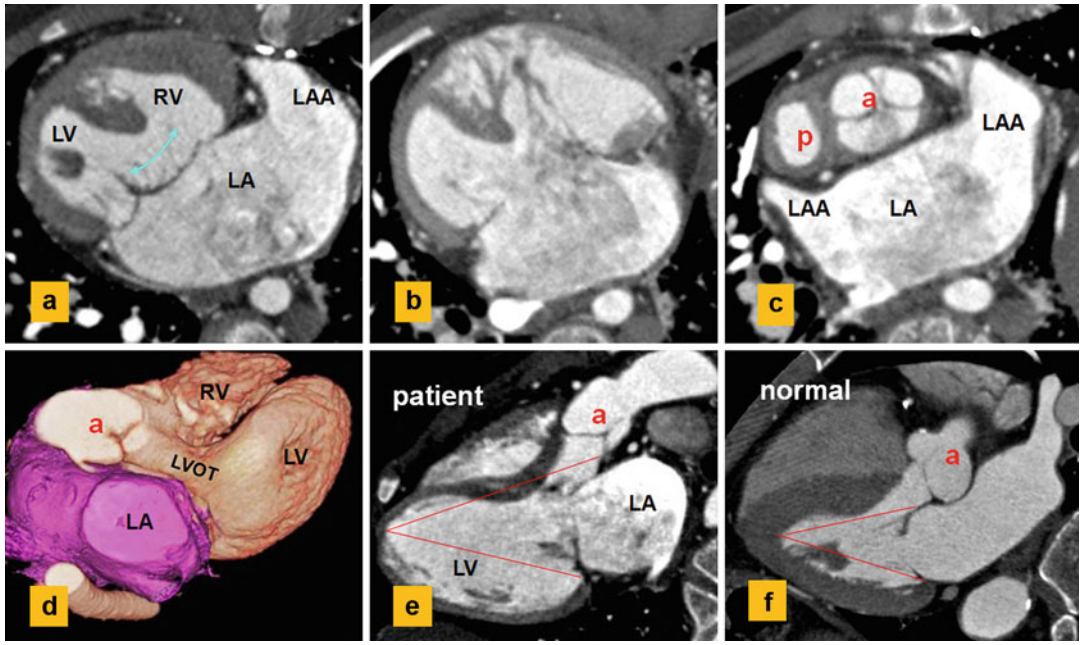

Fig. 13.17 CT images show a single atrium, left atrial isomerism, and dextrocardia. Status post-Fontan and main pulmonary artery exclusion. (**a**, **b**) Complete AVSD with a large inlet ventricular septal defect (*curved arrow*). (**c**) shows unwedging of the aortic root (*a*). (**d**, **e**) show elongation of the left ventricle (*LV*) outflow tract (*LVOT*) causing longer distance of the aortic valve to LV apex compared to the distance from apex to atrioventricular ring. Normally, the two distances are equal (**f**). (**f**) Normal example. *P* pulmonary, *LAA* left atrial appendage, *RV* right ventricle

the common valve and the crest of the interventricular septum. In a partial AVSD, the bridging leaflets fuse to the crest of the interventricular septum, leaving only an ostium primum ASD. They may also fuse with the atrial septum, leaving only a VSD. The potential for left-to-right shunting is related to the bridging leaflets being attached to the atrial septum, to the ventricular septum, or floating within the AVSD [77–80].

Another characteristic feature of AVSD is the anterior and rightward displacement of the aorta in relation to the common AV junction causing an "unwedged" aorta with a narrowed elongated left ventricle outflow tract (LVOT). LVOT elongation creates the characteristic "gooseneck deformity" on left ventriculography and unequal distances from the LV apex to the inlet and outlet valves. Normally, the two distances are equal (Fig. 13.17). Subaortic narrowing/stenosis is particularly notable in partial defects with an ostium primum ASD where the superior bridging leaflet is firmly fixed to the crest of the ventricular septum. Unwedging of aorta can lead to a displacement of the AV conduction tissue and its abnormality.

Most primum ASDs are relatively large and lead to right heart dilation. Because of the trileaflet nature of the left AV valve (the so-called cleft mitral valve), valvular regurgitation is common whereas valvular stenosis is rare [78]. A parachute-type or double-orifice "mitral" valve may be present [78]. Complex forms of AVSD are found in the majority of hearts with right atrial isomerism and in around half with left atrial isomerism. The former tends to have univentricular hearts, often with a common atrium, while the latter tends to have biventricular hearts [79] (Fig. 13.17). In atrial isomerism, the common AV valve usually has four leaflets: a large anterosuperior leaflet, two lateral leaflets, and a posteroinferior leaflet [80].

In most patients with AVSD, the ventricles are similarly sized (balanced AVSD). In a minority of cases, the common AV junction is committed to one ventricle leading to hypoplasia of the

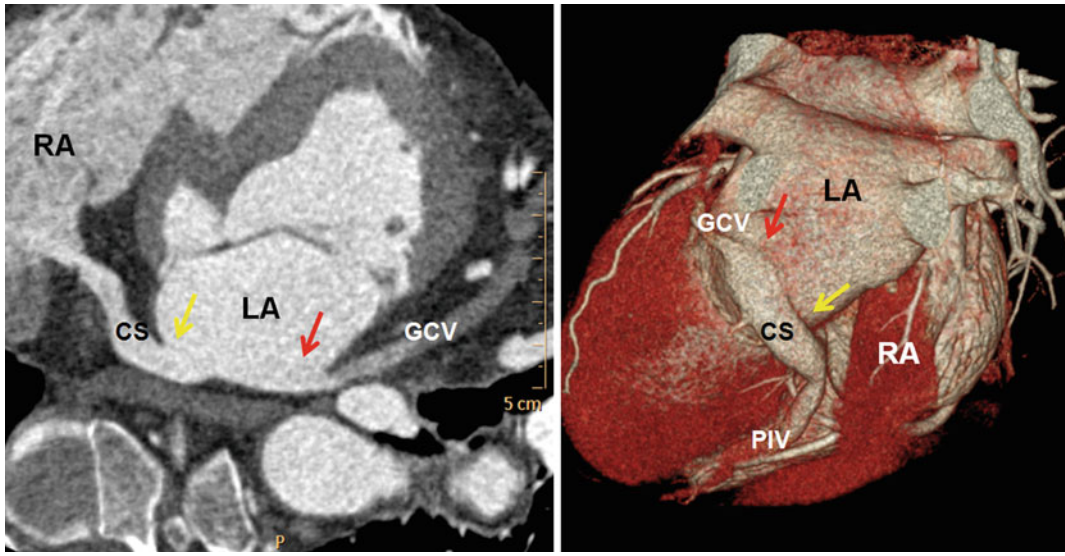

Fig. 13.18 Unroofed coronary sinus (*CS*) shown by CT. Large area of deficient CS roof (*between arrows*) is shown connecting its lumen with the left atrium (*LA*) cavity. No left superior vena cava was seen. The ostium of the CS connecting to the right atrium (*RA*) appears normal. *GCV* great cardiac vein, *PIV* posterior interventricular vein (Courtesy of Professor Se Hwan Kwon, College of Medicine, Kyung Hee University, Seoul, Republic of Korea)

opposing ventricle. Extreme commitment of the common AV junction to the left ventricle has been termed "double inlet LV with a common valve" [80]. Only a limited number of articles about MR and CT of AVSD exist. In one study of imaging analysis of AVSD, MRI was more accurate than echocardiography in predicting the size of the VSD and diagnosis of ventricular hypoplasia [81].

Fenestrated (Unroofed) Coronary Sinus

Anomalies of the coronary sinus may occur as isolated findings of little functional importance or as part of the spectrum of CHD findings. Fenestrated (unroofed) CS is rare and involves 1 % of all ASDs [82, 83]. Several anatomic variations have been described, ranging from complete absence of the walls between the CS and the left atrium to one or more partial fenestrations. In 2/3 of cases, partial communication is in the midportion and in 1/3 in the terminal portion of the CS (Fig. 13.18). In three-quarters of cases, there is either persistence of the left SVC or other findings of the CHD especially secundum ASD. It is relatively common in heterotaxy syndrome when there is isomerism of the left atrial appendages and in tricuspid atresia [84, 85] (see Chap. 31). In one series of partial CS fenestration, half of the cases were missed during previous cardiovascular surgery [84]. In adults, fenestrated CS is usually found incidentally as part of imaging workup of patients with history of surgery for CHD or as an isolated finding. Because of the small defect, the hemodynamic effect of the right-to-left shunting can be negligible. However, there is always the risk of stroke or brain abscess due to paradoxical embolism. Given the higher resolution and three-dimensional nature of reconstructed data, the diagnosis of CS fenestration may be easier in cardiac CT compared with MRI and echocardiography [86, 87].

ASD Closure

Indications for ASD closure are right atrial and right ventricular dilation, ASD size >1 cm, and Qp/Qs of 1.5 or greater. ASD closure is not recommended in severe pulmonary hypertension and very small defects. Small defects can be followed with imaging. Surgical closure is required for patients with ostium primum and sinus

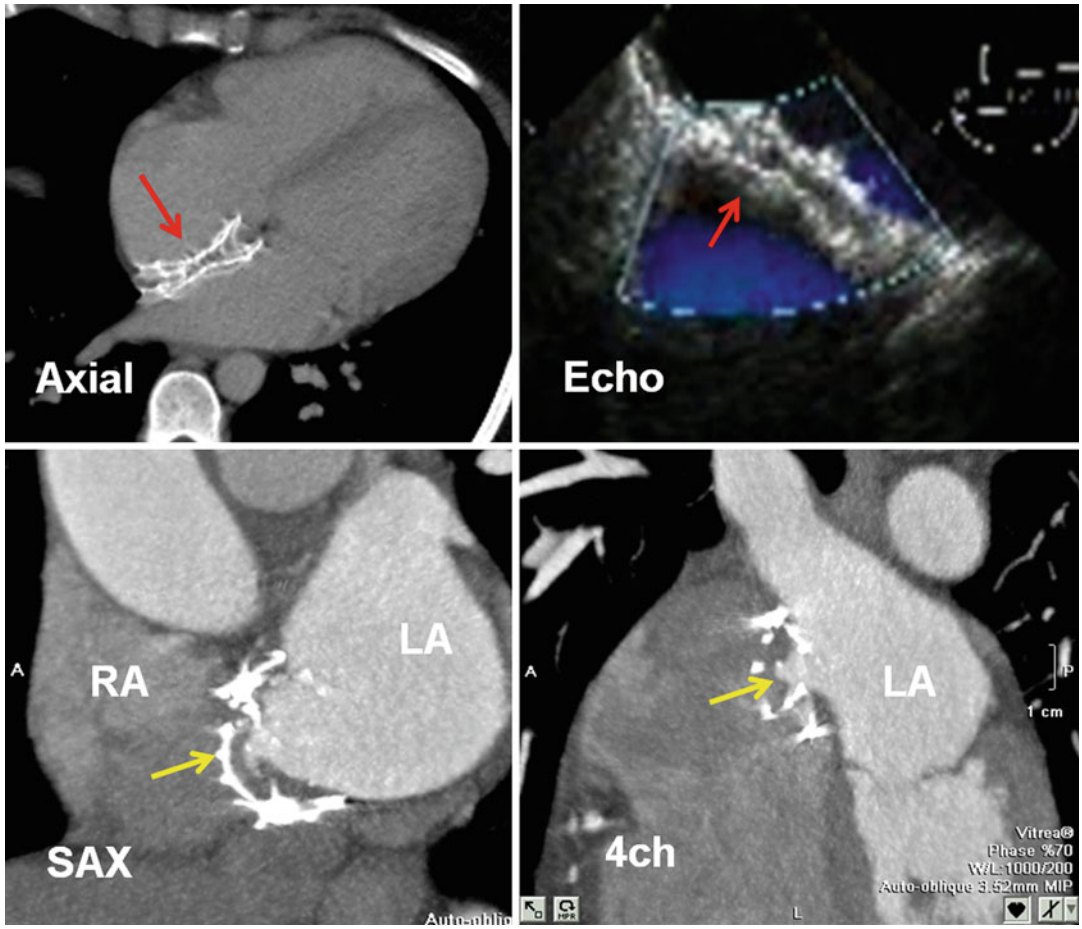

Fig. 13.19 Amplatzer septal occluders (*red arrows*) and Cardioseal device (*yellow arrows*) for ASD treatment are shown. *SAX* short axis, *4ch* four chamber, *LA* left atrium, *RA* right atrium

venosus ASDs as well as for patients with secundum ASDs with unsuitable morphology for device closure. A deficient rim of fossa ovalis and close proximity to the SVC, IVC, and CS may prevent successful closure [88, 89].

Different devices are available for ASD closure, although in the majority of centers the Amplatzer septal occluder and the Cardioseal device are used (Fig. 13.19). With the introduction of large Amplatzer devices (up to 40 m), the size of the defect no longer seems to be a limiting factor [89]. Device closure of secundum ASDs can produce rapid cardiac remodeling and decreased right atrial and ventricular volumes [90]. Residual small shunt after device closure is common and usually closes spontaneously in 1 year.

Both MR and CT have been used for pre- and post-transcatheter closure of ASDs and demonstrated some advantages over TEE [91, 92]. Demonstration of venous anomalous drainage is easier with these techniques. MDCT has been used as an alternative to TEE for evaluating Amplatzer septal occluders for ASD [92]. The metallic component of the occluder, which is a major problem for MRI and echocardiography, does not impair the diagnostic quality of MDCT scans (Fig. 13.19). MDCT is claimed to be helpful as it can reconstruct any plane owing to its volume image data nature and it is able to show residual defects, shunts, and device protrusions or migration that is not seen on TTE. MDCT is a good choice when TEE cannot provide convincing information. The most common

operation for sinus venosus defects consists of patch closure of the defect with concomitant baffling of any associated PAPVR into the left atrium [93] (Fig. 13.16). Correction of the superior variety of defects is less problematic, although it can be difficult to separate the venous streams without producing venous obstruction [93]. Sinoatrial node injury is another complication.

Ventricular Septal Defect

The most common form of CHD in childhood is the VSD. It is found as a part of complex cardiac malformations in 50 % of patients and in 20 % as an isolated lesion [93–96]. Due to spontaneous and surgical closure, it is less common in adults. Still in adults, it is the second most common CHD after bicuspid aortic valve. Anatomic knowledge of the ventricles and the ventricular septum is the prerequisite for understanding different types of VSD. Detailed anatomy and pertinent terminologies of the RV and RVOT are described in Chap. 10. In this chapter, the ventricular septum anatomy will be reviewed.

Anatomy of Ventricular Septum

The interventricular (IV) septum can be divided into two morphological components, the membranous septum and the muscular septum [7]. The membranous septum is part of septal components of the AV junction. The septal components of the AV junction are important because they conduct the cardiac impulse from the atria to the ventricles [97]. At the crux of the heart, there is an area where tricuspid valve is attached to the septum closer to the ventricular apex than the mitral valve (Fig. 13.20). This relationship is inverted in congenitally corrected transposition of the great arteries (ccTGA) and the distance is longer in Ebstein anomaly. In this region, the cavity of the right atrium is separated from that of the LV by the AV muscular sandwich, also known as muscular AV septum. As stated by Anderson et al. [97], this area is not a true septum and similar to the interatrial groove is only filled with the epicardial fibrofatty tissue of inferior pyramidal space sandwiched between the atrial wall and the ventricular musculature. This can be clearly shown by CT [98] (Fig. 13.21). The membranous septum is small and is located at the base of the heart below the right and noncoronary cusps of the aortic valve. The membranous ventricular septum is divided by the attachment of the septal leaflet of the tricuspid valve into two components: the AV portion separating the left ventricle from the right atrium and the IV portion, attached to the muscular septum. The relative sizes of the two components are variable and determined by the site of attachment of the septal leaflet of the tricuspid valve to the membrane and the height of the posterior aortic sinus. The membranous septum can be large in ccTGA. The central fibrous body lies superior and anterior to the muscular AV septum. The central fibrous body is made up by the right fibrous trigone and the membranous septum and fuses the annuli of the tricuspid, mitral, and aortic valves [97]. Of surgical importance is the close proximity of the conduction system of the heart to the membranous septum. The AV node is located in apex of the triangle of Koch of the right atrium (formed by Eustachian ridge, the CS ostium, and the septal leaflet of the tricuspid valve). From another perspective, the AV node is below the nadir of the noncoronary sinus of the aortic valve on the right atrial side of the central fibrous body. The bundle of His exists the AV node and penetrates the right fibrous trigone and runs along the inferior margin of the IV component of the membranous septum underneath the septal attachment of the tricuspid valve before dividing into the left and right bundle branches. The bundle of His can be damaged by the sutures during repair of a perimembranous VSD. The left bundle branch fans out over the septum while the right bundle branch courses as a single trunk below the medial papillary muscle complex and then to the inferior borders of the septal and moderator bands until it reaches the anterior papillary muscle where it distributes to innervate the RV. The conduction system can also be at risk at the superior edge of a muscular inlet VSD, where the conduction system runs in the muscle between the VSD and the membranous septum.

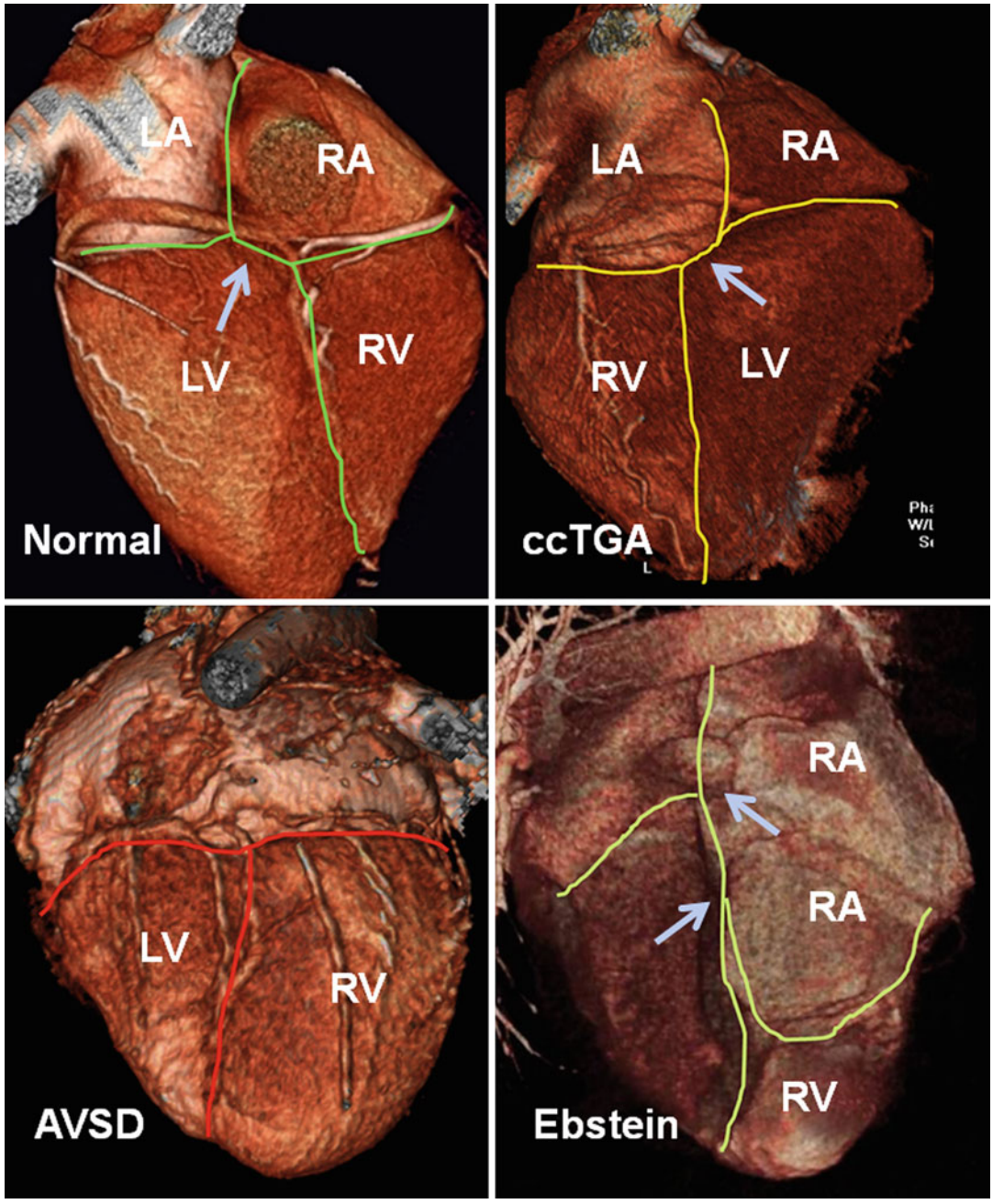

Fig. 13.20 External cardiac crux pattern in normal heart, congenitally corrected transposition of the great arteries (*ccTGA*), atrioventricular (AV) canal defect with single atrium, and Ebstein anomaly. External cardiac crux is an area in the posterior aspect of the heart where cardiac chambers show their maximum proximity (*arrow*). The vertical and horizontal lines in the cardiac crux are not perpendicular (*green lines*). In normal heart, the right AV groove is inferior to the left AV groove due to inferior position of the septal leaflet of tricuspid relative to the mitral valve. This relationship is reversed in ccTGA. There is no offset in the AV septal defect (*AVSD*) and the offset is huge in Ebstein due to apical migration of the tricuspid valve (*arrows*). *LA* left atrium, *LV* left ventricle, *RA* right atrium, *RV* right ventricle boundaries between heart chambers are shown by color line in each figure

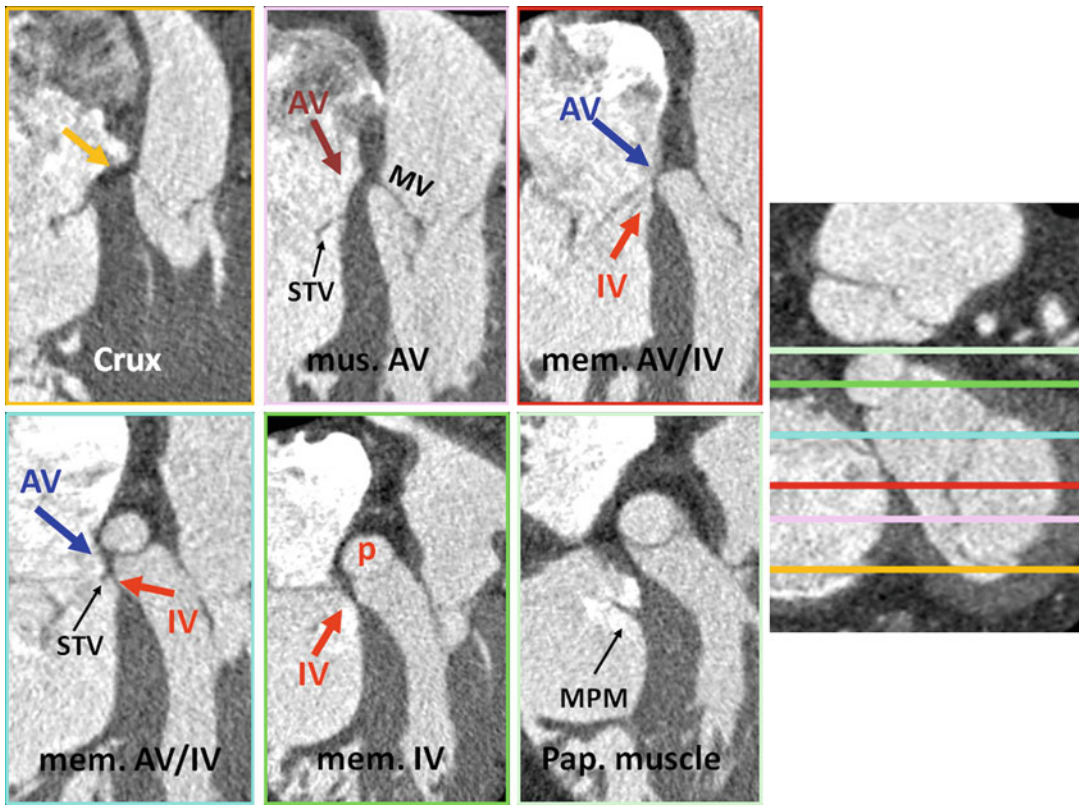

Fig. 13.21 The septal components of the atrioventricular (*AV*) junction. Four-chamber slices are reconstructed at the levels of internal cardiac crux, muscular (*mus.*) atrioventricular (*AV*) septum, membranous (*mem.*) AV septum, and membranous interventricular (*IV*) septum. Note the offset between the septal attachment of tricuspid valve (*STV*) and the mitral valve (*MV*) at muscular AV septum. The membranous septum itself is divided into two parts by the STV. Epicardial fibrofatty tissue is seen at the level of the cardiac crux sandwiched between the right atrial and left ventricular muscle walls (*mus. AV*). *MPM* medial papillary muscle, *p* posterior aortic sinus

The muscular septum can be divided into inlet, trabecular, and infundibular components. The inlet portion is inferoposterior to the membranous septum and extends from the AV junction to the chordal attachments of the AV valve. The trabecular component of septum is the largest part and extends to the apex. The infundibular septum separates the right and left ventricular outflow tracts.

Aneurysm of the Membranous Septum

The membranous septum can be thickened, perforated by one or many holes, or form an aneurysm. These are more likely to occur in the IV portion of the membranous septum in association with or as a result of a perimembranous defect. The etiology of this anomaly may be abnormal embryologic development or weakness of the affected tissues [99]. Aneurysms may limit intracardiac shunting and, in some cases, result in spontaneous defect closure. The characteristic outpouching or wind sock appearance on echocardiography or MRI results from aneurysmal distension to the right during ventricular systole (Fig. 13.7). Left-to-right shunt is usually shown only in systole (Fig. 13.22). Aneurysm of the IV membranous septum may be an uncommon occult cardiac source of systemic embolism [100]. Other associations include tricuspid regurgitation, obstruction to blood flow, endocarditis, and conduction disturbances [99].

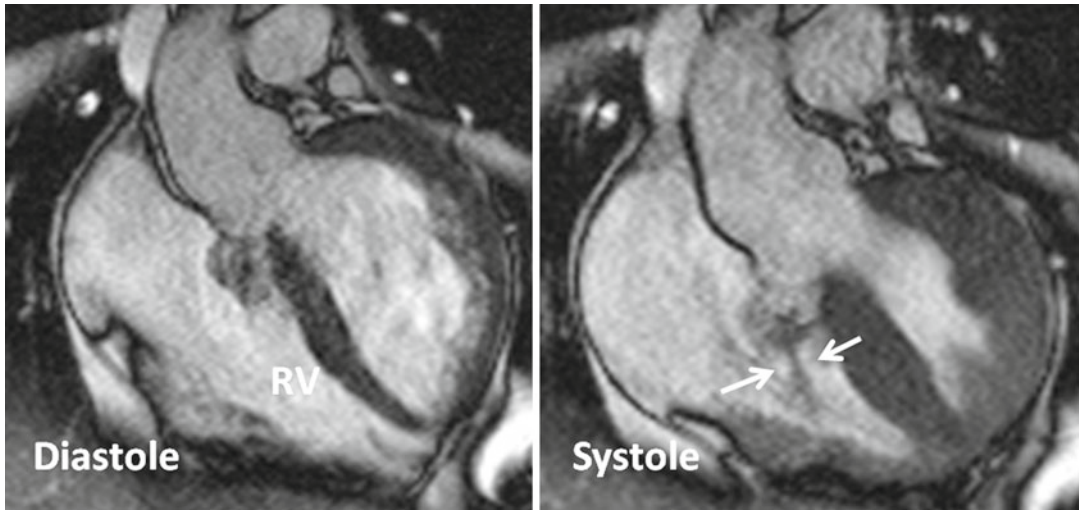

Fig. 13.22 Aneurysm of the interventricular membranous (*solid arrows*) with a small ventricular septal defect (*arrows*) best shown in systole. Aneurysms may limit intracardiac shunting and, in some cases, result in spontaneous defect closure. *RV* right ventricle

A defect in the AV membranous septum causing a shunt from the left ventricle to the right atrium is described as "Gerbode defect" [101, 102]. In congenital form, this usually represents a perimembranous VSD with a jet directed through a cleft in the tricuspid valve. An elongated sail-like anterior tricuspid leaflet in a perimembranous VSD may form an aneurysm and direct the shunt into right atrium. A consequence of this shunting can be right atrial enlargement. Acquired Gerbode defect has been described after bacterial endocarditis, trauma, and aortic root surgery (Fig. 13.23).

Classification of VSD

There are different classifications and nomenclature of VSDs, according to their location, that have been proposed and used [103, 104] (Fig. 13.24). Most classifications relate to the works done by Moulaert, Soto, and Anderson on cadaveric hearts [104, 105] and elegant echocardiography correlation on 280 cases of VSD later published by Sutherland et al. [106]. They divided VSDs into three groups: (1) perimembranous (70 %) including outlet (infundibular), muscular (trabecular), and inlet (AV canal defect) types, (2) subarterial (5 %), and (3) muscular including trabecular, outlet (infundibular), and inlet (25 %). A notable exception to this distribution is the high prevalence (30 %) of subarterial VSDs in the Asian population with VSDs [107].

Another popular classification was proposed by Capelli et al. based on two-dimensional (2D) echocardiography [108]. In their approach, the VSDs were simply grouped into subvalvular and muscular. The subvalvular group constitutes any VSDs partially bound by a valve and includes inlet, subtricuspid, subaortic, subarterial doubly committed, and subpulmonary. The muscular group was subclassified into outlet, central, and apical.

The most recent practical classification in use by the Society of Thoracic Surgeons (STS) is the one proposed by the American Heart Association Task Force on Practice Guidelines [96]: type 1 (conal, subpulmonary, infundibular, supracristal, and doubly committed juxta-arterial defects), type 2 (perimembranous, paramembranous, and conoventricular defects), type 3 (inlet and AV canal varieties), and type 4 (muscular VSDs).

Isolated defects of the membranous septum are surrounded by fibrous tissue without extension into adjacent muscular septum. These defects are uncommon in adults and probably are

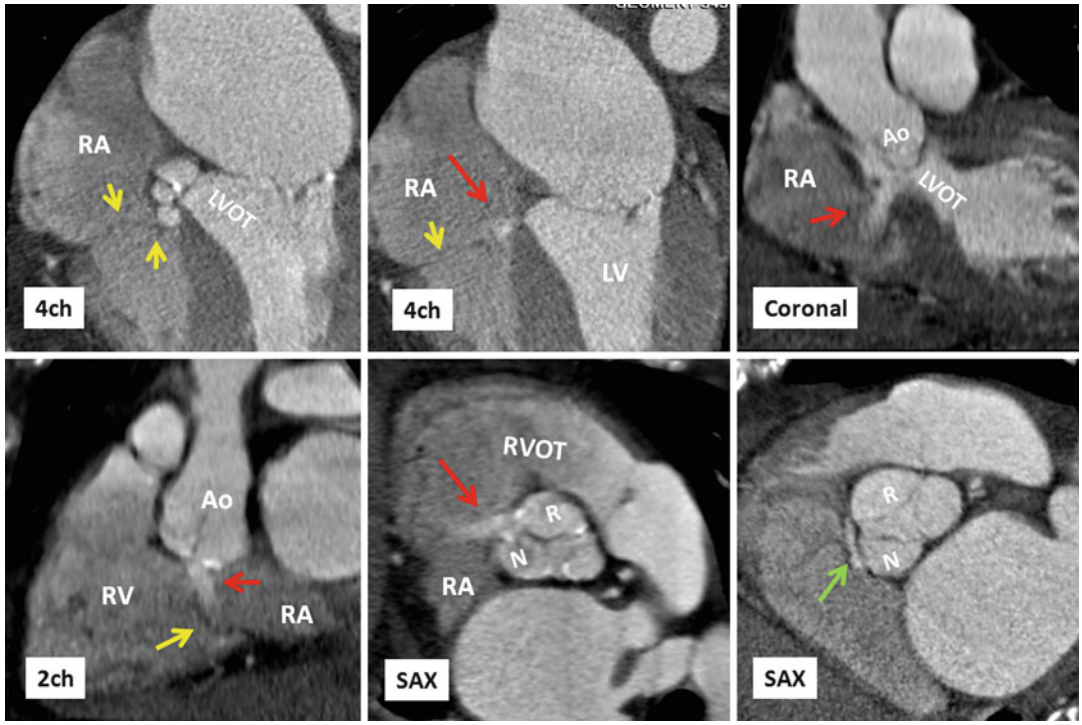

Fig. 13.23 Atrioventricular membranous defect (Gerbode) in a 73-year-old male with aortic valve disease. Calcified valve with vegetation and mild regurgitation was shown on echocardiography. Different projections of CT angiography show small membranous defect with shunt (*red arrows*) from the left ventricle (*LV*) into the right atrium (LA). The shunt was more obvious during diastole arising between the right coronary (*R*) and noncoronary (*N*) cusps. The level of tricuspid valve is shown by *yellow arrows*. Small collection of contrast (*green arrow*) between the aortic valve (*Ao*) and the RA is consistent with a small sinus tract. *LVOT* left ventricle outflow tract, *RVOT* right ventricle outflow tract, *RV* right ventricle, *4ch* four chamber, *2ch* two chamber, *SAX* short axis

sealed by tricuspid leaflet (Fig. 13.25). Defects that involve the membranous septum and surrounding muscles are called perimembranous, paramembranous, or infracristal. These are the most common VSDs and involve 70–80 % of cases [105]. Important criteria of diagnosis of perimembranous defects are subaortic location and fibrous continuity between the leaflets of the aorta and tricuspid valves (Fig. 13.26). Therefore, not every subaortic defect is perimembranous as it is common to see a fibrous tissue that separates the roof of defect from the aortic valve [109]. Subpulmonary extension occurs in large defects. Perimembranous defects are subpulmonary in hearts with discordant ventriculoarterial connection and there is fibrous continuity between the pulmonary and tricuspid valves. Perimembranous extensions of the defect are classified into the inlet, outlet, and muscular septa types. Large defects may involve all three components. The most common type is the outlet variant. Perimembranous outlet defects are located anterior to medial papillary muscle. Perimembranous inlet defects are also roofed by the AV valve and located posterior to the medial papillary muscle. Abnormalities of the tricuspid valve adjacent to a membranous or perimembranous VSDs can be in the form of an aneurysm partially or completely occluding the defect (Fig. 13.25). Although uncommon, prolapse of the right or noncoronary coronary sinus leaflets in perimembranous (subaortic) defects can cause aortic valve insufficiency (Fig. 13.27). This phenomenon is more common in subpulmonary infundibular VSDs.

Perimembranous trabecular defects are best seen at the most posterior aspect of a

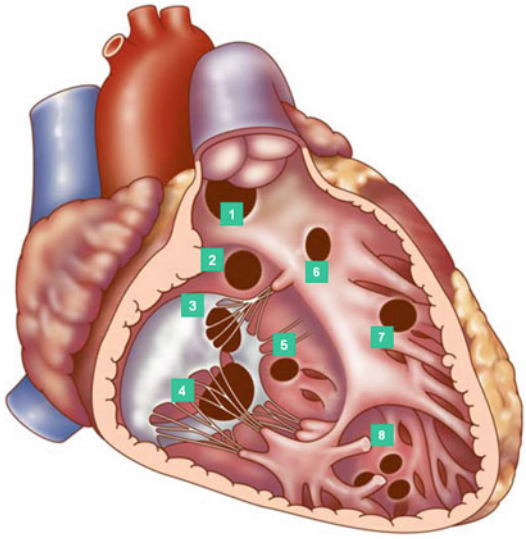

Fig. 13.24 VSD classification (right ventricular view). *1–4* are subvalvular defects. *1* Supracristal (doubly committed subarterial) defect. *2* Perimembranous outlet defect. *3* Perimembranous inlet defect. *4* Atrioventricular (septum primum) defect. *5–8* are muscular defects at inlet, outlet (infundibular) and anterior trabecular, and apical trabecular regions of the ventricular septum, respectively

four-chamber view of aortic root plane. In the normal heart, using two-dimensional echocardiography, it is difficult to locate the precise junction of membranous and trabecular septa but CT of the heart can easily localize it (Fig. 13.21). Blunting of the upper margin of the IV septum may indicate its involvement. Although perimembranous defect exists in isolation, it is most frequently associated with other defects (i.e., tetralogy of Fallot) (Fig. 13.26). From surgical point of view, the diagnosis of perimembranous VSD is important as it places the patient at risk of injury to conduction system at the time of surgery. The bundle of His passes along the inferior margin of perimembranous outlet VSD [109].

Perimembranous inlet defects (endocardial cushion defect) are roofed by the AV valve and characterized by absence of the AV muscular septum causing common level of insertion of the AV valve septal leaflets to central fibrous body (mitral-tricuspid continuity) (Fig. 13.28).

Muscular defects surrounded entirely by muscular rims may be subdivided into trabecular, outlet (infundibular), and inlet. Infundibular

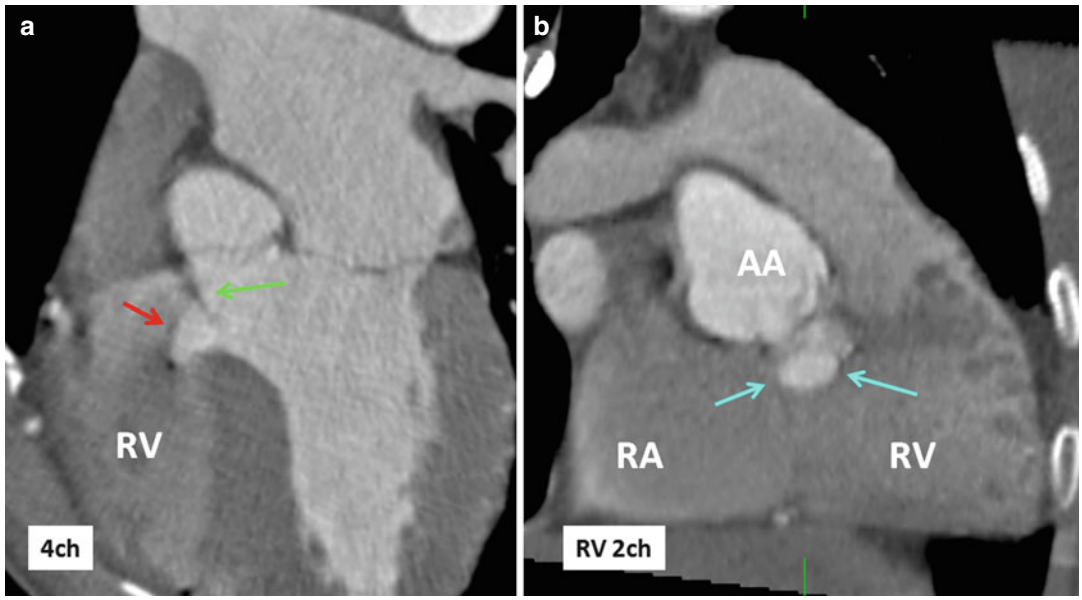

Fig. 13.25 (**a**) Four chamber and (**b**) 2 chamber of the right ventricle. Membranous VSD (*blue arrows*) protected and sealed by septal tricuspid leaflet (*red arrow*). Residual of the membrane is seen (*green arrow*). *AA* ascending aorta, *RA* right atrium, *RV* right ventricle, *4ch* four chamber, *2ch* two chamber

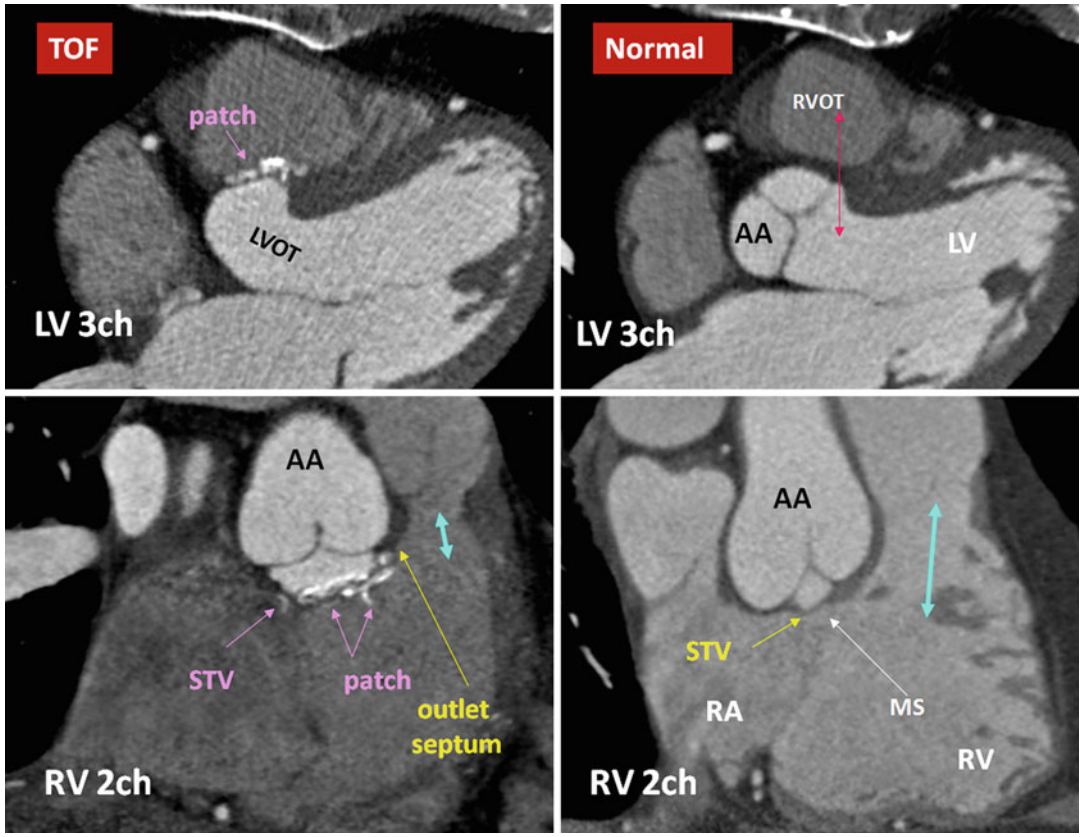

Fig. 13.26 Tetralogy of Fallot (*TOF*) versus normal heart. Left ventricle three-chamber (*LV 3ch*) and right ventricle two-chamber (*RV 2ch*) views of two subjects, one with repaired TOF and the second one with normal heart, are presented for comparison. In TOF, a subaortic perimembranous VSD is closed with a Dacron patch. The right ventricle outflow tract (*RVOT*) is short (*blue arrow*) and shows mildly thickened septoparietal trabeculations. No RVOT stenosis is seen (Eisenmenger defect). Malaligned outlet septum is seen displaced superiorly. The membranous septum (*MS*) is absent and the septal tricuspid (*STV*) leaflet is almost in fibrous continuity with the aortic leaflet. In 3ch view, the left ventricle outflow tract (*LVOT*) appears longer in TOF possibly due to dextroposition of the aortic root. Note the interventricular communication (closed by the patch) between the limbs of the septomarginal trabeculation. In normal heart, outlet septum is absent or involves a small portion of the crista supraventricularis crest (*double-headed red arrow*). *RA* right atrium, *RV* right ventricle, *LV* left ventricle, *AA* ascending aorta

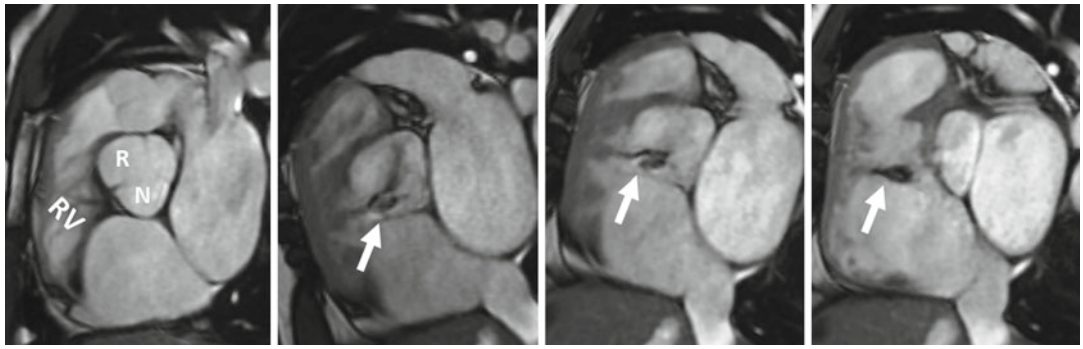

Fig. 13.27 A 35-year-old male with a small membranous VSD. Short axis MR images show aortic regurgitation between the right (*R*) and noncoronary (*N*) sinuses with the shunt (*arrows*) directed into the right ventricle (*RV*) through the membranous septum defect

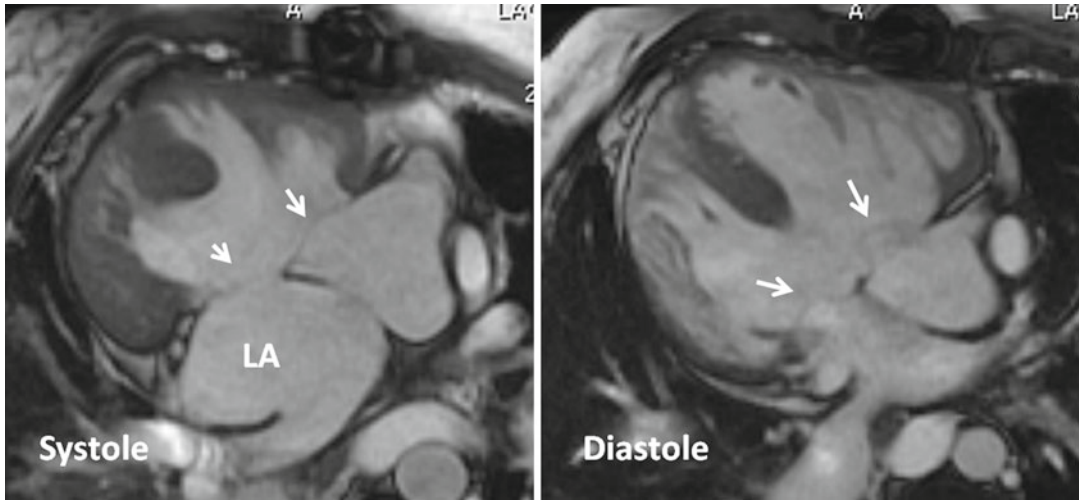

Fig. 13.28 Large perimembranous inlet (atrioventricular septal defect) with an intact atrial septum in a patient with dextrocardia, situs inversus, and azygos continuation of the inferior vena cava to the left superior vena cava. Note that the septal leaflets of the common atrioventricular valve (*arrows*) are attached at the same level to the central fibrous body

defects are the least common. Trabecular VSDs are the most common locations of muscular defects (Fig. 13.10). They are usually single but can be multiple and apical (Swiss cheese) [110]. Small VSDs in trabecular septum can be difficult to differentiate from myocardial clefts and large Thebesian sinuses (Fig. 13.29). The location of trabecular VSD can be subclassified as anterior, apical, and posterior [111]. The septomarginal trabeculation is the anatomic border between anterior muscular and posterior defects (Fig. 13.30). Apical defects are distal to the moderator band. Inlet muscular defects are posteriorly located beneath the medial papillary muscle but do not reach an arterial or AV valve, and there is normal pattern of septal AV valve insertions. Single trabecular defects and small multiple ("Swiss cheese") defects are difficult to find with echocardiography [106] and high-resolution cardiac CT may be the preferred method of diagnosis.

Defects in the infundibulum (conal, outlet, supracristal) can be muscular or subarterial. Outlet muscular VSD is found in the RVOT above or in a limb of septomarginal trabeculation. The superior border of this defect may extend up within the infundibular septum (Fig. 13.31). Infundibular muscular defect is best seen on short axis images at the level of RVOT. They can be small and easily be missed. Subarterial type of infundibular VSDs can be subpulmonary or doubly committed. Subpulmonary defects are often small and associated with prolapse of the right coronary cusp in older oriental patients, but is unusual in children <4 years of age. In subpulmonary defects, the infundibular septum exists but appears deficient. In doubly committed, subarterial defect is directly roofed by conjoined aortic and pulmonary valves at the same level (in 15 %, an offset exists) which are in fibrous continuity with no "outlet septum" between them [112] (Fig. 13.32). The inferior margin of defect is formed by the crest of the trabecular septum. Posteriorly, it may extend into the membranous septum (type 1) or may be covered by a muscle ridge (type 2). They are best seen on coronal or four-chamber planes of the heart passing through the aortic root. A fibrous raphe between the two arterial valves may be seen in doubly committed VSD that should not be mistaken with a hypoplastic outlet septum [112]. This defect may be isolated or as part of tetralogy of Fallot. In tetralogy of Fallot, the defect is mainly subaortic and pulmonary valve stenosis coexists. Subpulmonary VSD is an integral component of the Taussig-Bing anomaly (double outlet

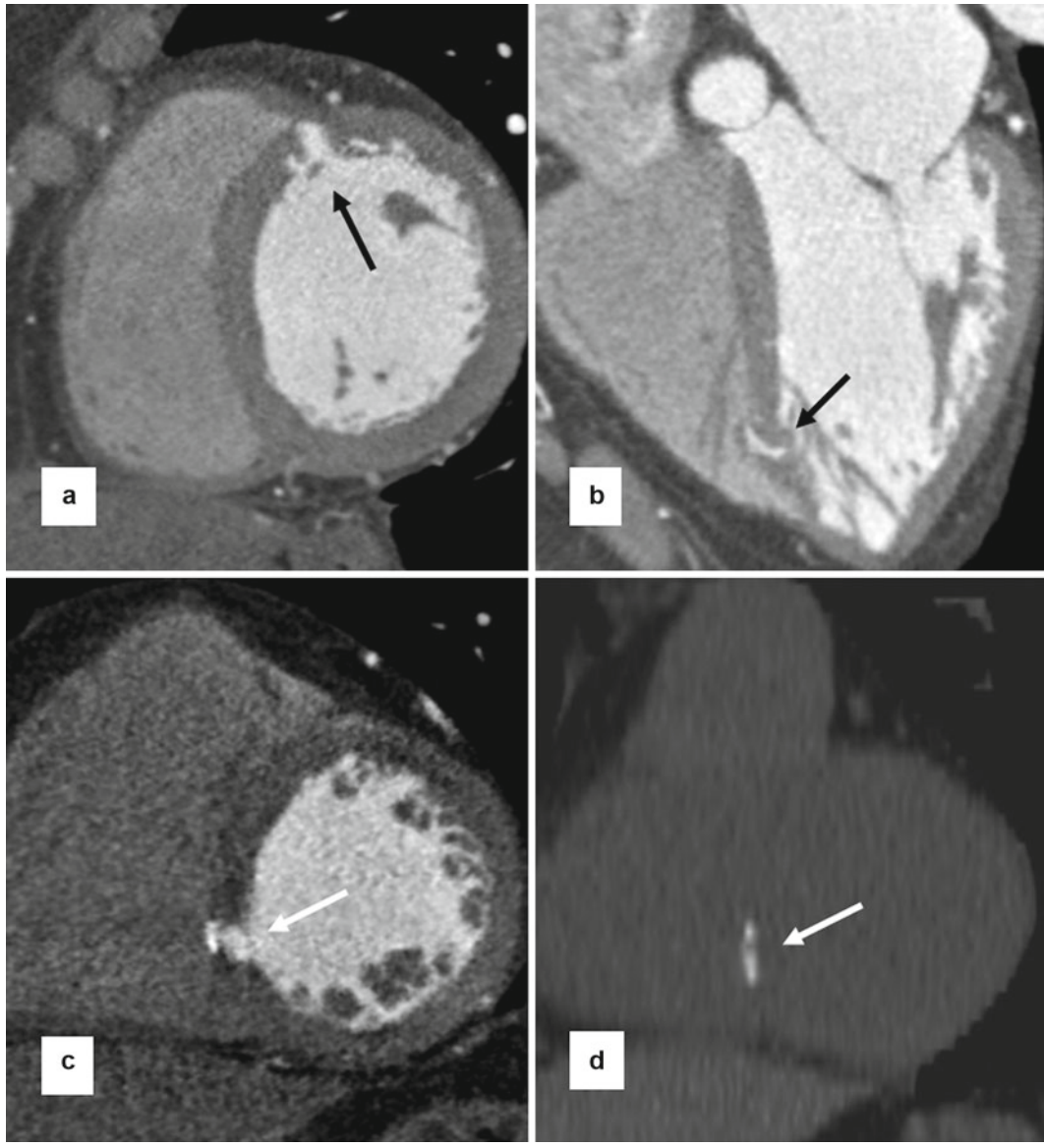

Fig. 13.29 Left ventricular septum filling defects. (**a**) Short axis CT shows diverticular appearance of a large Thebesian sinus (*arrow*). (**b**) Large venous sinus (*arrow*) in the apical septum. (**c**) Post- and (**d**) pre-contrast CT scans show residual cleft related to ventricular septal defect closing patch (*arrows*)

RV with subpulmonary VSD). It is important to remember that in normal heart, the outflow tracts are separated by ventriculoinfundibular fold and a true muscular septum cannot be identified or is very small [5] (Chap. 10). The subpulmonary infundibulum which supports the leaflets of the pulmonary valve produces the normal offsetting between the leaflets of the aortic and pulmonary valves. In the presence of a VSD between the two outlets, the septal morphology will be different and is characterized by the presence of a muscular bar named "outlet septum." This outlet septum forms the superior margin of the VSD and varies in length and thickness. In doubly committed defect, the ventriculoinfundibular fold is absent [112] (Fig. 13.32).

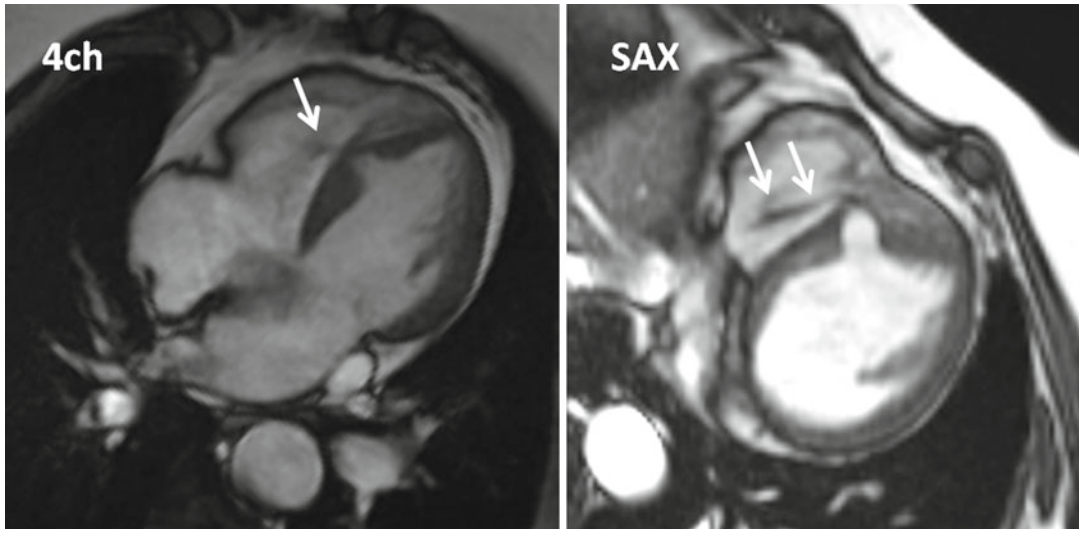

Fig. 13.30 Four-chamber (*4ch*) and short axis (*SAX*) cine images of cardiac MR show muscular ventricular septal defect in the anterior midportion of the trabecular septum causing a small left-to-right shunt (*arrows*)

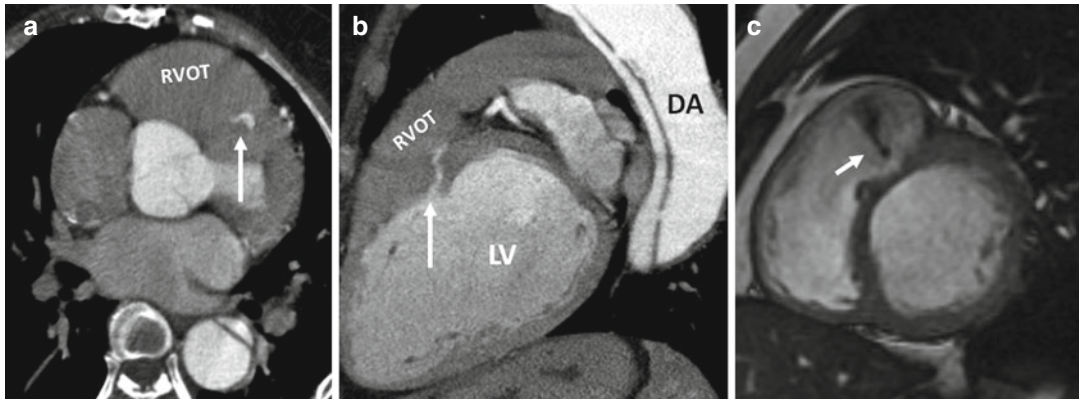

Fig. 13.31 (**a**, **b**) Axial and long axis CT images show that a small infundibular muscular ventricular septal defect (*arrows*) was incidentally found in this patient who admitted for treatment of descending thoracic aortic (*DA*) dissection. (**c**) Short axis MRI in a different patient shows the jet of left-to-right shunt into the right infundibulum (*small arrow*). *RVOT* right ventricle outflow tract, *LV* left ventricle

Infundibular and perimembranous outlet defects can be associated with various degrees of malalignment of the "outlet septum" and the remainder of the ventricular septum. Anterior or posterior deviation of the infundibular septum can cause right or left outflow tract obstruction, respectively. Fibroelastic bar or membranous tissue protruding from the left septal surface into the subaortic region can cause discrete short segment subaortic stenosis [113, 114]. In a VSD with subaortic stenosis, the rate of aortic arch interruption is higher. Subaortic stenosis may develop later after closure of VSD and repair of the aortic anomaly [115].

Imaging and Hemodynamic Assessment of VSDs

In addition to location, number, and sizes of defects, imaging data should include assessment of ventricular function and search for aortic valve

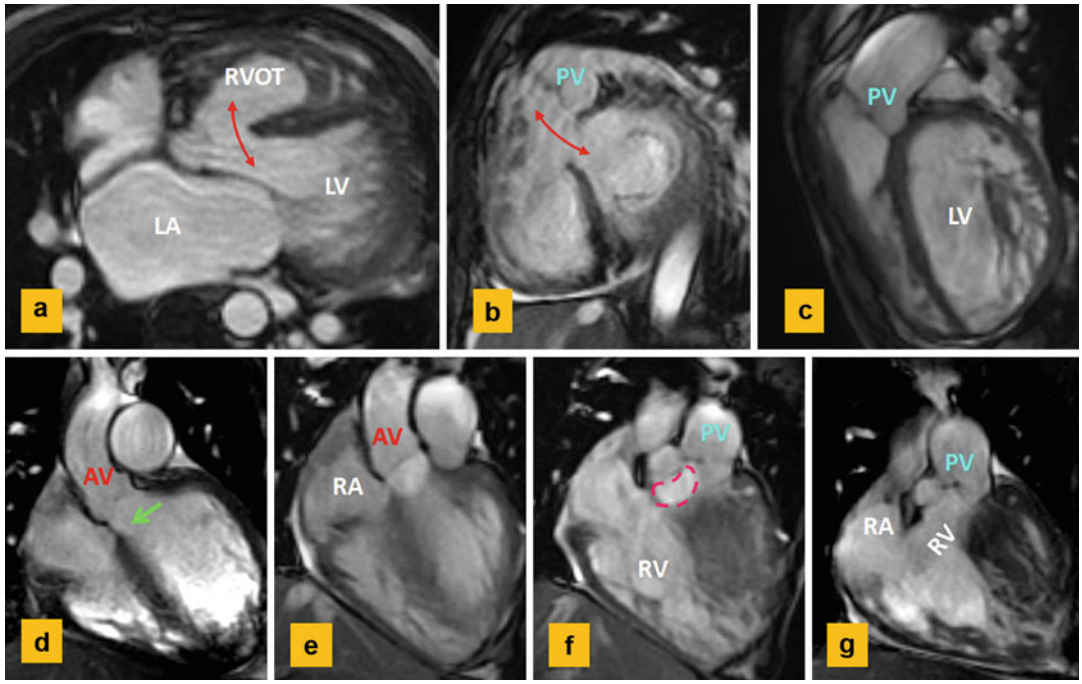

Fig. 13.32 Cine views of MRI in a 54-year-old male with left heart failure and pulmonary hypertension showing a subarterial ventricular septal defect (VSD). (**a**) Axial view shows the VSD and hypertrophied right ventricle outflow tract (*RVOT*). (**b**) Short axis at the level of mitral valve shows large VSD defect (*red arrow*). (**c**) Lateral view shows intact pulmonary valve (*PV*). There subpulmonary infundibulum is not developed. (**d**–**g**) are coronal images parallel to ventricular septum. The membranous septum is intact (*green arrow*). The VSD is mainly subaortic (**e**, **f**) with some subpulmonary component. The VSD area demarcated by *red circle* in (**f**), measured at 3.8 cm^2. The aortic valve (*AV*) and PV are at the same level. *RA* right atrium, *RV* right ventricle, *LA* left atrium, *LV* left ventricle

prolapse and/or regurgitation, outflow tract obstruction, and tricuspid regurgitation. Residual or recurrent VSDs in imaging studies of adults with repaired CHD are not uncommon. In adults with poor echocardiographic windows, TEE may be necessary. CT and MR are mainly recommended to confirm the anatomy of unusual VSDs such as inlet or apical defects not well seen by echocardiography as well as for the assessment of coexisting abnormalities in the pulmonary arteries, the pulmonary veins, and the aorta [109]. Diagnosis and correct localization of the perimembranous defects require detailed evaluation of the anatomic structures around them and multiplanar reconstructions to show their spatial location in the heart. For example, demonstration of fibrous continuity between the aorta and tricuspid valves is the key element for diagnosis of perimembranous defects. This can be best achieved with cardiac CT with special attention to technique of contrast administration to optimally show structures on both sides of the defect. A high-resolution imaging technique is required to show a small muscle bar between the valves and to distinct a muscular defect from a perimembranous defect.

Similar to ASD, noninvasive hemodynamic analysis of VSD can be obtained with echocardiography or MRI. CT can indirectly evaluate the amount of shunt by measuring the systemic and pulmonary flows using a retrospective ECG-gated technique. Direct measurement of shunt volume is not possible with CT; however, in selected cases, real-time visualization of the shunt can be achieved using a dynamic contrast-enhanced scan at the level of shunt. This will increase total radiation dose and is not routinely recommended.

The shunt volume in a VSD is determined largely by the size of the defect and the

pulmonary vascular resistance. Without pulmonary hypertension or obstruction to the right ventricle, the direction of shunt is left to right and if large enough can cause left heart volume overload. In the setting of elevated pulmonary vascular resistance, RVOT obstruction due to hypertrophied muscles, or pulmonary stenosis, the shunt volume is limited and may be right to left, depending on the difference in pressure. Eisenmenger syndrome results from long-term left-to-right shunting, usually at higher shunt volumes [116] (Chap. 33).

VSD Closure

Muscular VSDs can undergo spontaneous closure as a result of muscular occlusion. Swiss cheese defects cannot close spontaneously and require surgery. The mechanism of closure of perimembranous defects is by apposition of tricuspid valve tissue, with or without formation of a septal aneurysm. Infundibular defects (doubly committed and subpulmonary) can close by prolapse of the right aortic cusp [117].

Spontaneous closure is otherwise rare. The pathophysiology of a VSD is determined by the size and location of defect. In restrictive VSD, the defect is smaller than the aortic annulus. In this type, the direction and volume of the shunt depends on the difference in systolic pressures of the ventricles [118]. Restrictive VSDs can be small or moderate in size. Small VSD is defined as <1 cm in size and left-to-right shunt of <50 % in the absence of pulmonary hypertension or pulmonary stenosis. The most common small defects in adults are perimembranous and subarterial [117]. Isolated small VSDs are considered benign and only need prophylaxis treatment for a low risk of endocarditis. Moderate-sized restrictive defects allow a large left-to-right shunt to cause left-sided volume overload, characterized by left atrium and left ventricle dilatation. Some pulmonary hypertension can exist [118]. In nonrestrictive VSD, the defect is large and ventricular pressures may equalize. The direction and volume of this shunt is determined by the difference in pulmonary and systemic vascular resistance. A nonrestrictive VSD is characterized by a large left-to-right shunt, left ventricle volume overload, and pulmonary hypertension resulting in Eisenmenger syndrome.

Generally, a Qp:Qs of 1.5:1 to 2:1, ventricular enlargement, pulmonary hypertension, or aortic regurgitation is an indication for surgery or transcatheter closure using Amplatzer VSD occluder [119–122]. Most common VSD surgeries in adults are perimembranous (70 %) and subarterial (25 %) [119].

Large apical muscular VSDs complicate management decisions, particularly when they occur in association with other congenital cardiac defects. Surgery for apical muscular VSDs is often suboptimal owing to difficulties in defect visualization, residual shunting, and ventricular dysfunction. Transcatheter closure is an alternative treatment [123].

Aortic cusp prolapse and aortic regurgitation can occur in more than 30 % of subarterial VSDs particularly in lesions larger than 5 mm. Aortic regurgitation is usually mild. It is more common in subpulmonary defect than subaortic perimembranous [107, 122]. In Lun et al. study, the coronary cusp prolapse in subpulmonic VSD was limited to the right cusp, and those in subaortic VSD were the right cusp, noncoronary cusp, or both [120]. Early surgical repair of the defect has been advocated. Subarterial defects <5 mm are usually asymptomatic and may incidentally be found during imaging workup [120] (Fig. 13.27).

Patent Ductus Arteriosus

Ductus arteriosus is a vascular connection between the aorta distal to the origin of the left subclavian artery and the superior margin of main pulmonary artery near the origin of the left pulmonary artery (Fig. 13.33). It originates from the distal left sixth embryonic arch and closes spontaneously within 48 h after birth. Persistence of the ductus after 3 months is called PDA [3, 124]. The incidence has been estimated to be as high as 1 in 500 and it is more common in females [125].

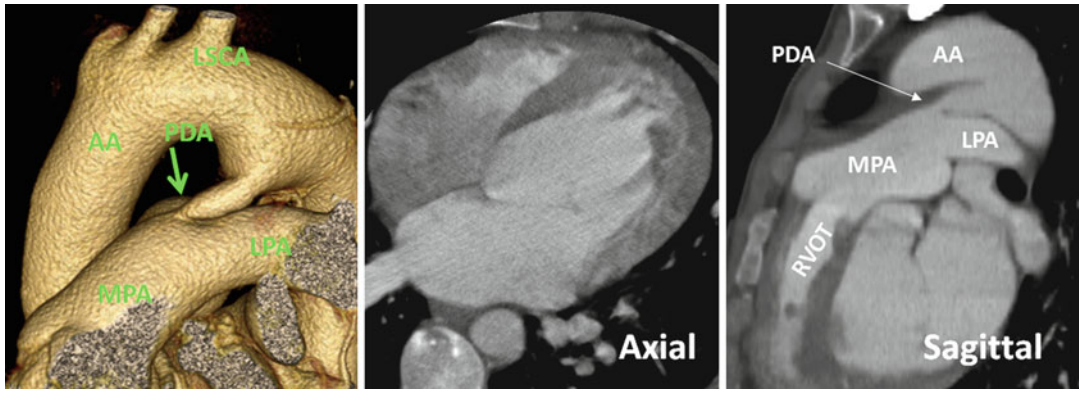

Fig. 13.33 Typical findings of patent ductus arteriosus (*PDA*). The PDA extends between the aorta distal to the origin of the left subclavian artery (*LSCA*) and the main pulmonary artery (*MPA*) near branching of the left pulmonary artery (*LPA*). It is usually less than 5 mm in diameter at the entrance into the MPA. Its origin from the aorta is larger and can be aneurysmal as shown in this case. There is volume overload of the left heart, hypertrophy of the right ventricle outflow tract (*RVOT*), and enlargement of the pulmonary arteries. *AA* ascending aorta

Clinical manifestations are usually determined by the size of PDA and the degree of left-to-right shunting. Regardless of the size, complications may arise, and imaging diagnosis is important. Long-standing left-to-right shunting results in pulmonary overcirculation, left heart volume overload, and progressive increase in pulmonary vascular resistance. In later stages, congestive heart failure or Eisenmenger syndrome can develop. It is not uncommon to find a small PDA in a patient with other congenital heart malformations (Fig. 13.34). A previously silent PDA may become symptomatic when combined with acquired conditions such as calcific aortic stenosis or ischemic heart disease [3]. Turbulent flow through the PDA can rarely lead to endothelial injury, complicated by infective or noninfective endocarditis and septic emboli [126].

Imaging diagnosis of a suspected PDA in adults can be difficult. Conversely, it is not uncommon to discover a silent PDA on routine CT or MR examinations. The information provided by imaging, such as the size, calcification, and morphology of the duct as well as the amount of left-to-right shunt, is crucial to the planning of optimal treatment. Different angiographic morphologies of PDA are classified by Krichenko et al. [127]. The most common morphology is "conical" with the aortic side larger than the pulmonary side (Fig. 13.33). Other variants include very short, long, tubular, and fusiform.

Traditionally, the initial noninvasive diagnostic investigation is performed with Doppler echocardiography [128]. In children, the size and morphology of the PDA can be predicted using Doppler echocardiography, but such assessment is not often possible in adults and MRI or CT may be required. TEE allows accurate diagnosis of shunt but it may not be the best technique for direct visualization of the PDA. Air in the left main bronchus can cause difficulty for TEE visualization of the PDA (Fig. 13.35). Intrabronchial balloon catheter filled with saline is used to overcome this limitation during intraoperative TEE [129]. Transcatheter occlusion has become the therapy of choice for treatment of PDA [130]; however, noninvasive imaging of PDA and judgment of indications for coil occlusion remain challenging. PDA closure is indicated for symptomatic adults with significant left-to-right shunting and for asymptomatic patients with significant shunting and evidence of left heart enlargement [3].

Both CT and MRI are accurate for morphological analysis of the PDA [131]. They both are useful for the assessment of associated abnormalities of the aortic arch such as vascular ring and right-sided aortic arch (Fig. 13.33). Demonstration of additional intracardiac lesions and anomalous venous return is easier with CT or MR. CT can

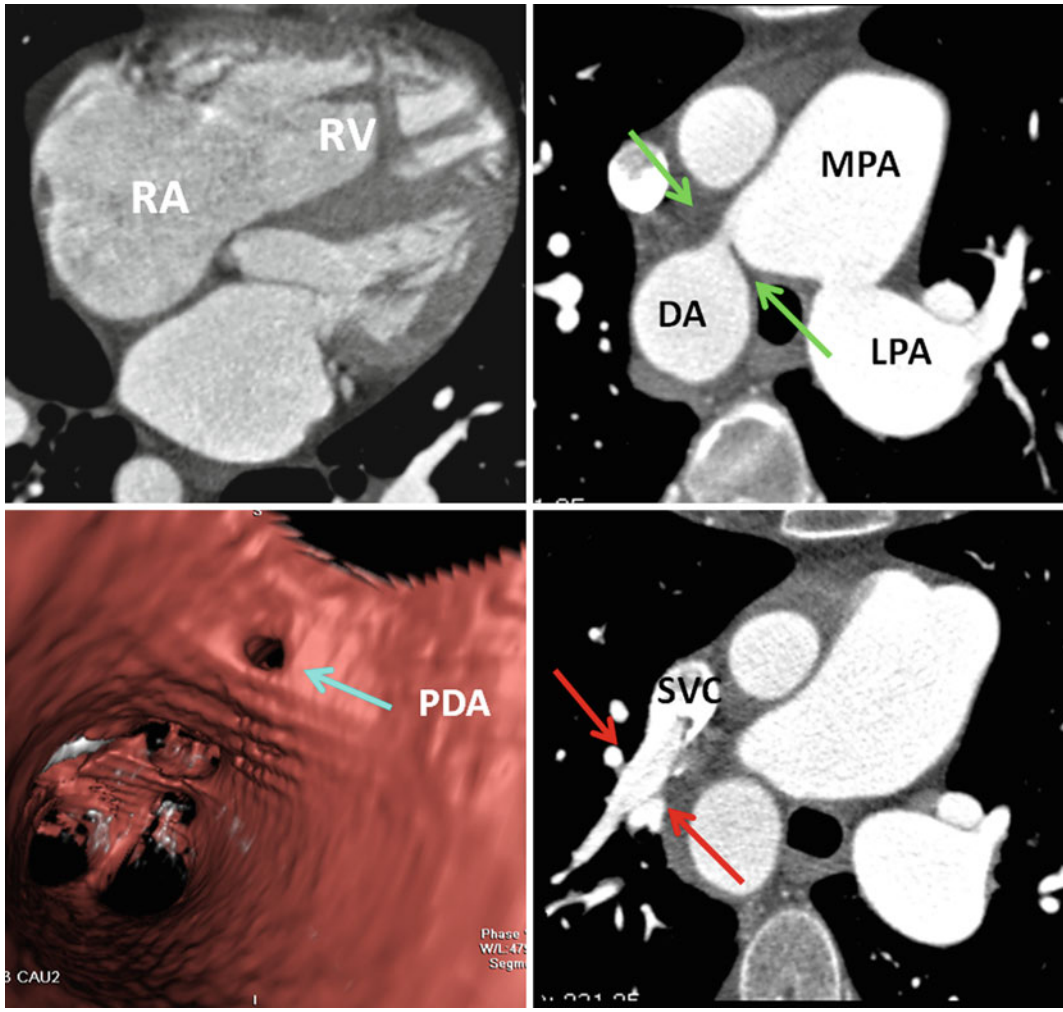

Fig. 13.34 A 37-year-old female scanned to further evaluate for right heart enlargement shown by echocardiography. Echo was reported negative for intracardiac shunt. CT angiography shows enlargement of the right atrium (*RA*), the right ventricle (*RV*), and the pulmonary arteries. Findings are consistent with pulmonary hypertension. A small short PDA was seen between a right-sided descending aorta (*DA*) and the main pulmonary artery (*MPA*) (*green arrows*). The origin of PDA is more toward the right pulmonary artery not the left pulmonary artery because of the right-sided position of the DA. The PDA orifice is clearly shown in CT endoscopy view of the aorta (*blue arrow*). Three anomalous pulmonary veins were found draining the right upper lung into the superior vena cava (*SVC*), one of those is shown in this case (*red arrow*). No intracardiac shunt was seen. It was concluded that pulmonary hypertension was the result of left-to-right shunting *arrows* at the level of anomalous pulmonary venous return rather caused by the small PDA. *LPA* left pulmonary artery

show calcification of the ductus better than MRI [131]. Patients with a heavily calcified duct or a duct exhibiting distortion or aneurysmal changes are not suitable candidates for surgery [132]. In large shunts, endovascular closure may also pose problems such as residual shunt or migration of the device [133]. In this situation, some reported endovascular stent graft as the preferred method of treatment [134]. Comprehensive imaging of aorta in these cases can be done with CT. Using

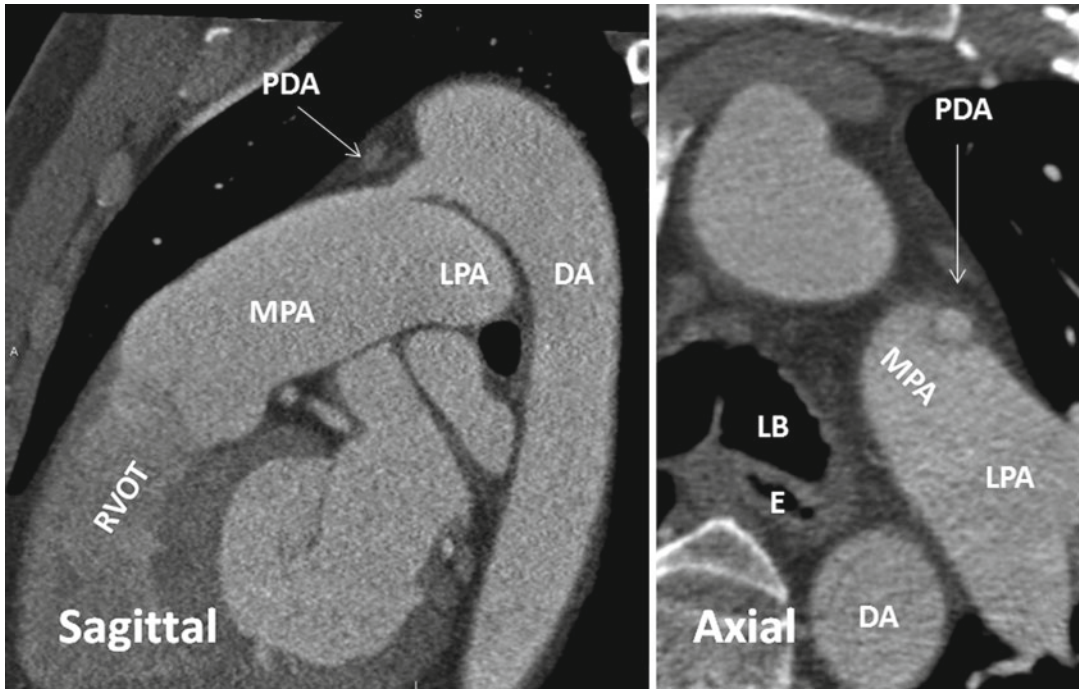

Fig. 13.35 The relation of the PDA with adjacent structures. The PDA is directed toward the main pulmonary artery (*MPA*). The left bronchus (*LB*) is interposed between the esophagus (*E*) and the left pulmonary vessels causing difficulty in visualization of the PDA orifice during transesophageal echocardiography. *DA* descending aorta, *LPA* left pulmonary artery, *RVOT* right ventricle outflow tract

CT anatomic relationship of the PDA and the left main bronchus can be reviewed before undertaking transcatheter closure, bearing in mind the assistance that the tracheal air shadow provides a fixed landmark during the transcatheter procedures (Fig. 13.34). Virtual endoscopy using CT data has been described as a useful technique in the assessment and treatment of PDA [135]. The anatomy of the orifice of the ductus and spatial relations of adjacent structures from both the aortic and pulmonary sides can be shown (Fig. 13.33). The mean angiographic diameter of the narrowest portion of a PDA can be as small as 3.2 (± 1.0) mm [127]. For this, high-resolution CT with at least 0.5-mm beam collimation is suggested to study these patients. To obtain high-quality images, an ECG-gated technique is preferred [131]. Dynamic assessment of the PDA shunt is possible with 64 or 320 slice scanners [136]. Overall, shunt analysis can be optimally performed with MRI or echocardiography. The jet of flow secondary to a PDA is directed preferentially toward the main pulmonary artery. For accurate results, collection of data with PC MRI should be perpendicular to direction of the PDA flow (Fig. 13.36). In PDA patients with high pulmonary vascular resistance and slow flow, the shunt may be very difficult to demonstrate. Additional image findings include ventricular septal flattening, right ventricular hypertrophy, high-velocity pulmonary regurgitation, tricuspid regurgitation, and left heart enlargement. Aneurysm of the ductus arteriosus is more common in children. In adult, it can be confused both clinically and radiologically with other masses in the aorticopulmonary window [137]. Large aneurysm can cause left vocal cord paralysis due to compression of the recurrent laryngeal nerve.

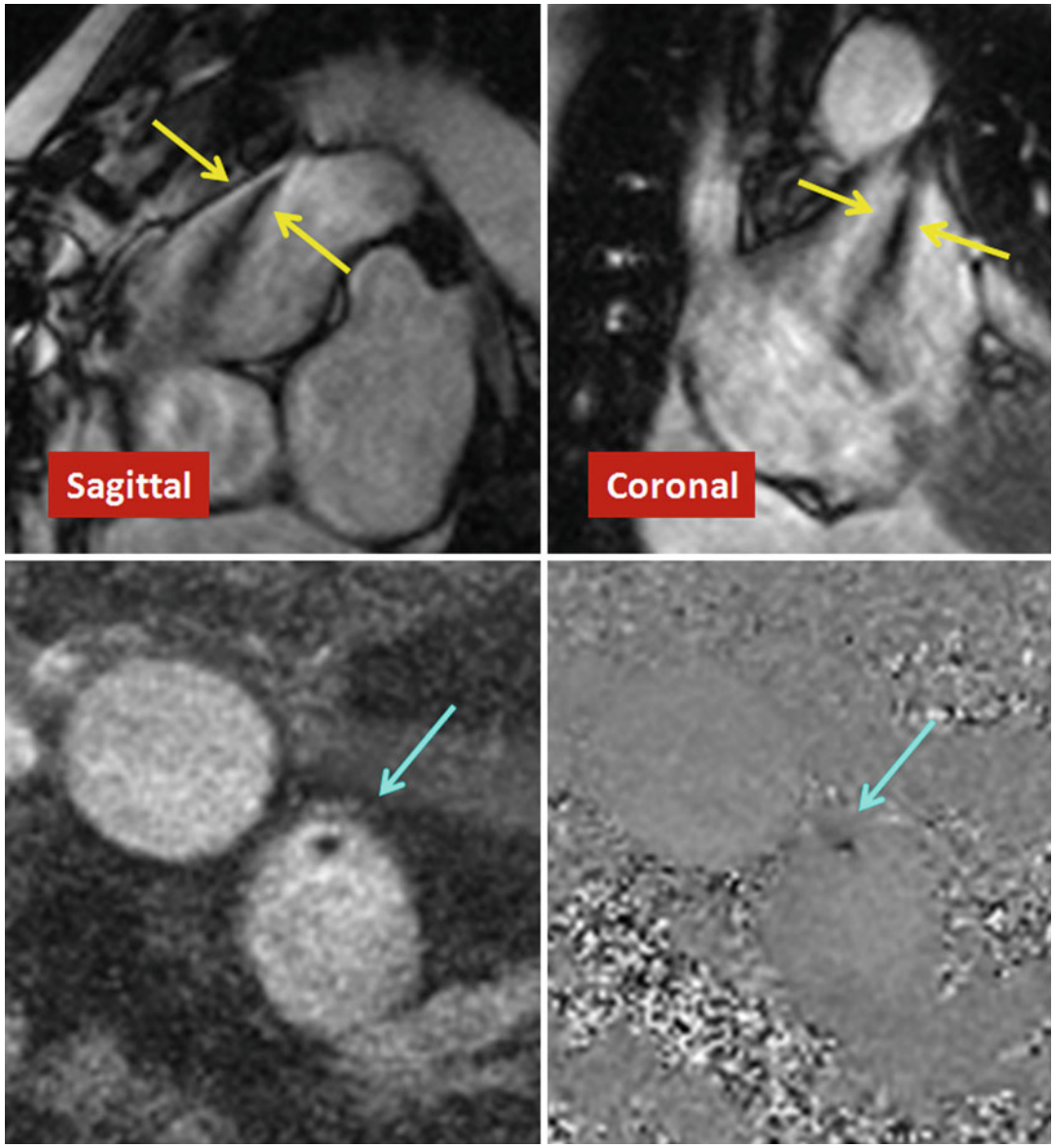

Fig. 13.36 MRI shows a small PDA (measured at 3 mm diameter) between the aorta and the main pulmonary artery. *Upper row* images are sagittal and coronal orthogonal cine images obtained for accurate localization of the shunt. *Lower row* demonstrates phase and magnitude MR images obtained through the shunt. There was a continuous left-to-right flow through the PDA with an easily identifiable jet into the main pulmonary artery (*yellow arrows*). Peak velocity through the PDA as measured with PC MR (*blue arrows*) was between 4.5 and 5.0 m/s. The main pulmonary artery is enlarged (4 cm). The heart was otherwise normal

References

1. Webb G, Gatzoulis M. Atrial septal defects in the adult: recent progress and overview. Circulation. 2006;114:1645–53.
2. Minette MS, Sahn DJ. Ventricular septal defects. Circulation. 2006;114:2190–7.
3. Schneider DJ, Moore JW. Patent ductus arteriosus. Circulation. 2006;114:1873–82.
4. Harley HR. The sinus venosus type of interatrial septal defect. Thorax. 1958;13(1):12–27.
5. Anderson RH, Webb S, Brown NA. Clinical anatomy of the atrial septum with reference to its developmental components. Clin Anat. 1999;12:362–74.

6. Anderson RH, Brown NA, Webb S. Development and structure of the atrial septum. Heart. 2002;88:104–10.
7. Anderson RH, Brown NA. The anatomy of the heart revisited. Anat Rec. 1996;246(1):1e7.
8. Thompson T, Evans W. Paradoxical embolism. Quart J Med. 1930;23:135–40.
9. Hagen PT, Scholz DG, Edwards WD. Incidence and size of patent foramen ovale during the first 10 decades of life: an autopsy study of 965 normal hearts. Mayo Clin Proc. 1984;59:17–20.
10. Webster MW, Chancellor AM, Smith HJ, et al. Patent foramen ovale in young stroke patients. Lancet. 1988;8601:11–2.
11. Homma S, Di Tullio MR, Sacco RL, Mihalatos D, Li Mandro G, Mohr JP. Characteristics of patent foramen ovale associated with cryptogenic stroke: a biplane transesophageal echocardiographic study. Stroke. 1994;25:582–6.
12. Saremi F, Channual S, Raney A, et al. Imaging of patent foramen ovale with 64-section multidetector CT. Radiology. 2008;249(2):483–92.
13. Ho SY, McCarthy KP, Rigby ML. Morphological features pertinent to interventional closure of patent oval foramen. J Interv Cardiol. 2003;16(1):33–8.
14. Natanzon A, Goldman ME. Patent foramen ovale: anatomy versus pathophysiology – which determines stroke risk? J Am Soc Echocardiogr. 2003;16(1):71–6.
15. Mohrs OK, Petersen SE, Erkapic D, Victor A, Schlosser T, Nowak B, Kauffmann G, Voigtlaender T, Kauczor HU. Dynamic contrast-enhanced MRI before and after transcatheter occlusion of patent foramen ovale. AJR Am J Roentgenol. 2007;188:844–9.
16. Nusser T, Hoher M, Merkle N, et al. Cardiac magnetic resonance imaging and transesophageal echocardiography in patients with transcatheter closure of patent foramen ovale. J Am Coll Cardiol. 2006;48:322–9.
17. Thomson LE, Crowley AL, Heitner JF, et al. Direct en face imaging of secundum atrial septal defects by velocity-encoded cardiovascular magnetic resonance in patients evaluated for possible transcatheter closure. Circ Cardiovasc Imaging. 2008; 1(1):31–40.
18. Sun JP, Stewart WJ, Hanna J, Thomas JD. Diagnosis of patent foramen ovale by contrast versus color Doppler by transesophageal echocardiography: relation to atrial size. Am Heart J. 1996;131(2): 239–44.
19. Kim YJ, Hur J, Shim CY, et al. Patent foramen ovale: diagnosis with multidetector CT – comparison with transesophageal echocardiography. Radiology. 2009; 250(1):61–7.
20. Koenig P, Cao QL, Heitschmidt M, Waight DJ, Hijazi ZM. Role of intracardiac echocardiographic guidance in transcatheter closure of atrial septal defects and patent foramen ovale using the Amplatzer device. J Interv Cardiol. 2003;16(1):51–62.
21. Graham LN, Melton IC, MacDonald S, Crozier IG. Value of CT localization of the fossa ovalis prior to transseptal left heart catheterization for left atrial ablation. Europace. 2007;9(6):417–23.
22. Chiari H. Uber Netzbildungcn im rechten Vorhof des Herzens. Beitr Pathol Anat. 1897;22:1–10.
23. Gresham GA. Networks in the right side of the heart. Br Heart J. 1957;19:381–6.
24. Bhatnagar KP, Nettleton GS, Campbell FR, Wagner CE, Kuwabara N, Muresian H. Chiari anomalies in the human right atrium. Clin Anat. 2006;19(6):510–6.
25. Goedde TA, Conetta D, Rumisek JD. Chiari network entrapment of thromboemboli: congenital inferior vena cava filter. Ann Thorac Surg. 1990;49:317–8.
26. Schneider B, Hofmann T, Justen MH, Meinertz T. Chiari's network: normal anatomic variant or risk factor for arterial embolic events? J Am Coll Cardiol. 1995;26(1):203–10.
27. Schneider B, Hanrath P, Vogel P, Meinertz T. Improved morphologic characterization of atrial septal aneurysm by transesophageal echocardiography: relation to cerebrovascular events. J Am Coll Cardiol. 1990;16:1000–9.
28. Zabalgoitia-Reyes M, Herrerra C, Ghandi DK, Mehlman DJ, McPherson DD, Talano JV. A possible mechanism for neurologic ischemic events in patients with atrial septal aneurysm. Am J Cardiol. 1990; 66:761–4.
29. Mattioli AV, Aquilina M, Oldani A, Longhini C, Mattioli G. Atrial septal aneurysm as a cardioembolic source in adult patients with stroke and normal carotid arteries. A multicentre study. Eur Heart J. 2001; 22(3):261–8.
30. Mugge A, Daniel WG, Angermann C, et al. Atrial septal aneurysm in adult patients. A multicenter study using transthoracic and transesophageal echocardiography. Circulation. 1995;91(11):2785–92.
31. Schuchlenz HW, Weihs W, Horner S, Quehenberger F. The association between the diameter of a patent foramen ovale and the risk of embolic cerebrovascular events. Am J Med. 2000;109:456–62.
32. Olivares-Reyes A, Chan S, Lazar EJ, et al. Atrial septal aneurysm: a new classification in two hundred five adults. J Am Soc Echocardiogr. 1997; 10:644–56.
33. Pearson AC, Nagelhout D, Castello R, Gomez CR, Labovitz AJ. Atrial septal aneurysm and stroke: a transesophageal echocardiographic study. J Am Coll Cardiol. 1991;18:1223–9, 99.
34. Hanley PC, TajiK AJ, Hynes JK, et al. Diagnosis and classification of atrial septal aneurysm by two-dimensional echocardiography: report of 80 consecutive cases. J Am Coll Cardiol. 1985;6:1370–82.
35. Schuchlenz HW, Saurer G, Weihs W, Rehak P. Persisting eustachian valve in adults: relation to patent foramen ovale and cerebrovascular events. J Am Soc Echocardiogr. 2004;17(3):231–3.
36. Ley S, Ley-Zaporozhan J, Kreitner KF, et al. MR flow measurements for assessment of the pulmonary, systemic and bronchosystemic circulation: impact of different ECG gating methods and breathing schema. Eur J Radiol. 2007;61(1):124–9.
37. Beerbaum P, Korperich H, Barth P, Esdorn H, Gieseke J, Meyer H. Noninvasive quantification of left-to-right shunt in pediatric patients: phase-contrast cine mag-

netic resonance imaging compared with invasive oximetry. Circulation. 2001;103:2476–82.
38. O'Donnell M. NMR blood flow using multiecho, phase contrast sequences. Med Phys. 1985;12:59–64.
39. Chatzimavroudis GP, Zhang H, Halliburton SS, et al. Clinical blood flow quantification with segmented k-space magnetic resonance phase velocity mapping. J Magn Reson Imaging. 2003;17:65–71.
40. Boehrer JD, Lange RA, Willard JE, Grayburn PA, Hillis LD. Advantages and limitations of methods to detect, localize, and quantitate intracardiac left-to-right shunting. Am Heart J. 1992;124:448–55.
41. Daniel WC, Lange RA, Willard JE, Landau C, Hillis LD. Oximetric versus indicator dilution techniques for quantitating intracardiac left-to-right shunting in adults. Am J Cardiol. 1995;75:199–200.
42. Cigarroa RG, Lange RA, Hillis LD. Oximetric quantitation of intracardiac left-to-right shunting: limitations of the Qp/Qs ratio. Am J Cardiol. 1989;64:246–7.
43. Tang C, Blatter DD, Parker DL. Accuracy of phase-contrast flow measurements in the presence of partial volume effects. J Magn Reson Imaging. 1993;3:377–85.
44. Lotz J, Meier C, Leppert A, Galanski M. Cardiovascular flow measurement with phase-contrast MR imaging: basic facts and implementation. Radiographics. 2002;22(3):651–71.
45. Andersen AH, Kirsch JE. Analysis of noise in phase contrast MR imaging. Med Phys. 1996;23:857–69.
46. Hundley WG, Li HF, Lange RA, et al. Assessment of left-to-right intracardiac shunting by velocity-encoded, phase-difference magnetic resonance imaging: a comparison with oximetric and indicator dilution techniques. Circulation. 1995;91:2955–60.
47. Ley S, Fink C, Puderbach M, Zaporozhan J, et al. MRI Measurement of the hemodynamics of the pulmonary and systemic arterial circulation: influence of breathing maneuvers. AJR Am J Roentgenol. 2006;187(2):439–44.
48. Stahlberg F, Thomsen C, Sondergaard L, Henriksen O. Pulse sequence design for MR velocity mapping of complex flow: notes on the necessity of low echo times. Magn Reson Imaging. 1994;12:1255–62.
49. Kondo C, Caputo GR, Semelka R, Foster E, Shimakawa A, Higgins CB. Right and left ventricular stroke volume measurements with velocity en-coded cine MR imaging: in vitro and in vivo validation. AJR Am J Roentgenol. 1991;157:9–16.
50. Hoeper MM, Tongers J, Leppert A, Baus S, Maier R, Lotz J. Evaluation of right ventricular performance with a right ventricular ejection fraction thermodilution catheter and magnetic resonance imaging in patients with pulmonary hypertension. Chest. 2001;120:502–7.
51. Powell AJ, Tsai-Goodman B, Prakash A, Greil GF, Geva T. Comparison between phase-velocity cine magnetic resonance imaging and invasive oximetry for quantification of atrial shunts. Am J Cardiol. 2003;91:1523–5, A1529.
52. Mohiaddin RH, Underwood R, Romeira L, et al. Comparison between cine magnetic resonance velocity mapping and first-pass radionuclide angiocardiography for quantitating intracardiac shunts. Am J Cardiol. 1995;75:529–32.
53. Esmaeili A, Hohn R, Koch A, Vogl TJ, Hofstetter R, Abolmaali N. Assessment of shunt volumes in children with ventricular septal defects: comparative quantification of MR flow measurements and invasive oximetry. Clin Res Cardiol. 2006;95:523–30.
54. Evans AJ, Iwai F, Grist TA, et al. Magnetic resonance imaging of blood flow with a phase subtraction technique. Invest Radiol. 1993;28:109–15.
55. Goldberg A, Jha S. Phase-contrast MRI and applications in congenital heart disease. Clin Radiol. 2012;67(5):399–410.
56. Mymin D, Sharma GP. Total and effective coronary blood flow in coronary and noncoronary heart disease. J Clin Invest. 1974;53:363–73.
57. Debl K, Djavidani B, Buchner S, et al. Quantification of left-to-right shunting in adult congenital heart disease: phase-contrast cine MRI compared with invasive oximetry. Br J Radiol. 2009;82:386e91.
58. Blom NA, Ottenkamp J, Jongeneel TH, DeRuiter MC, Gittenberger-de Groot AC. Morphogenetic differences of secundum atrial septal defects. Pediatr Cardiol. 2005;26(4):338–43.
59. Biben C, Weber R, Kesteven S, et al. Cardiac septal and valvular dysmorphogenesis in mice heterozygous for mutations in the homeobox gene Nkx2-5. Circ Res. 2000;87:888–9.
60. Maeno YV, Benson LN, McLaughlin PR, Boutin C. Dynamic morphology of the secundum atrial septal defect evaluated by three dimensional transoesophageal echocardiography. Heart. 2000;83:673–7.
61. Ferreira SMAG, Ho SY, Anderson RH. Morphological study of defects of the atrial septum within the oval fossa: implications for transcatheter closure of left-to-right shunt. Br Heart J. 1992;67:316–20.
62. Ross DN. The sinus venosus type of atrial septal defect. Guy's Hosp Rep. 1956;105:376–81.
63. Davia JE, Cheitlin MD, Bedynek JL. Sinus venosus atrial septal defect. Am Heart J. 1973;85:177–85.
64. Brickner ME, Hillis LD, Lange RA. Congenital heart disease in adults- first of two parts. N Engl J Med. 2000;342:256–63.
65. Van Praagh S, Carrera ME, Sanders SP, Mayer JE, Van Praagh R. Sinus venosus defects: unroofing of the right pulmonary veins-anatomic and echocardiographic findings and surgical treatment. Am Heart J. 1994;128:365–79.
66. al Zaghal AM, Li J, Anderson RH, Lincoln C, Shore D, Rigby ML. Anatomical criteria for the diagnosis of sinus venosus defects. Heart. 1997;78(3):298–304.
67. Butts RJ, Crean AM, Hlavacek AM, et al. Veno-venous bridges: the forerunners of the sinus venosus defect. Cardiol Young. 2011;21(6):623–30.
68. Crystal MA, Al Najashi K, Williams WG, Redington AN, Anderson RH. Inferior sinus venosus defect: echocardiographic diagnosis and surgical approach. Thorac Cardiovasc Surg. 2009;137(6):1349–55.
69. Kafka H, Mohiaddin RH. Cardiac MRI and pulmonary MR angiography of sinus venosus defect and

partial anomalous pulmonary venous connection in cause of right undiagnosed ventricular enlargement. AJR Am J Roentgenol. 2009;192:259–66.
70. Swan HJC, Kirklin JW, Becu LM, Wood EH. Anomalous connection of right pulmonary veins to superior vena cava with interatrial communications. Hemodynamic data in eight cases. Circulation. 1957;16:54–66.
71. Vogel M, Berger F, Kramer A, Alexi-Meshkishvili V, Lange PE. Incidence of secondary pulmonary hypertension in adults with atrial septal or sinus venosus defects. Heart. 1999;82:30–3.
72. Kronzon I, Tunick PA, Freedberg RS, Trehan N, Rosenzweig BP, Schwinger ME. Transesophageal echocardiography is superior to transthoracic echocardiography in the diagnosis of sinus venosus atrial septal defect. J Am Coll Cardiol. 1991; 17:537–42.
73. Pascoe RD, Oh JK, Warnes CA, Danielson GK, Tajik AJ, Seward JB. Diagnosis of sinus venosus atrial septal defect with transesophageal echocardiography. Circulation. 1996;94:1049–55.
74. Ferrari VA, Scott CH, Holland GA, Axel L, Sutton MS. Ultrafast three-dimensional contrast enhanced magnetic resonance angiography and imaging in the diagnosis of partial anomalous pulmonary venous drainage. J Am Coll Cardiol. 2001;37:1120–8.
75. Valente AM, Sena L, Powell AJ, Del Nido PJ, Geva T. Cardiac magnetic resonance imaging evaluation of sinus venosus defects: comparison to surgical findings. Pediatr Cardiol. 2007;28:51–6.
76. Plymale J, Kolinski K, Frommelt P, Bartz P, Tweddell J, Earing MG. Inferior sinus venosus defects: anatomic features and echocardiographic correlates. Pediatr Cardiol. 2013;34:322–6.
77. Anderson RH, Ho SY, Falcao S, et al. The diagnostic features of atrioventricular septal defect with common atrioventricular junction. Cardiol Young. 1998;8(1):33–49.
78. Smallhorn JF. Cross-sectional echocardiographic assessment of atrioventricular septal defect: basic morphology and preoperative risk factors. Echocardiography. 2001;18:415–32.
79. Arisawa J, Morimoto S, Ikezoe J, et al. Cross sectional echocardiographic anatomy of common atrioventricular valve in atrial isomerism. Br Heart J. 1989;62(4):291–7.
80. De Tommasi S, Daliento L, Ho SY, Macartney FJ, Anderson RH. Analysis of atrioventricular junction, ventricular mass, and ventriculoarterial junction in 43 specimens with atrial isomerism. Br Heart J. 1981;45(3):236–47.
81. Parsons JM, Baker EJ, Anderson RH, et al. Morphological evaluation of atrioventricular septal defects by magnetic resonance imaging. Br Heart J. 1990;64(2):138–45.
82. Quaegebeur J, Kirklin JW, Pacifico AD, Bargeron Jr LM. Surgical experience with unroofed coronary sinus. Ann Thorac Surg. 1979;27(5):418–25.
83. Ootaki Y, Yamaguchi M, Yoshimura N, Oka S, Yoshida M, Hasegawa T. Unroofed coronary sinus syndrome: diagnosis, classification, and surgical treatment. J Thorac Cardiovasc Surg. 2003;126(5):1655–6.
84. Attenhofer Jost CH, Connolly HM, Danielson GK, Dearani JA, Warnes CA, Jamil Tajik A. Clinical features and surgical outcome in 25 patients with fenestrations of the coronary sinus. Cardiol Young. 2007;17(6):592–600.
85. Matsuwaka R, Tomokuni T, Ishikawa S, Watanabe F, Matsushita T, Matsuda H. Partially unroofed coronary sinus associated with tricuspid atresia: an important associated lesion in the Fontan operation. Eur J Cardiothorac Surg. 1987;1:180–2.
86. Brancaccio G, Miraldi F, Ventriglia F, Michielon G, Di Donato RM, De Santis M. Multidetector-row helical computed tomography imaging of unroofed coronary sinus. Int J Cardiol. 2003;91:251–3.
87. Chaturvedi A, Dubinsky TJ, Maki JH. MR findings of a rare defect, coronary sinus ASD. Int J Cardiovasc Imaging. 2012;28(2):429–30.
88. Du ZD, Koenig P, Cao QL, et al. Comparison of transcatheter closure of secundum atrial septal defect using the Amplatzer septal occluder associated with deficient versus sufficient rims. Am J Cardiol. 2002;90:865–9.
89. Fischer G, Stieh J, Uebing A, et al. Experience with transcatheter closure of secundum atrial septal defects using the Amplatzer septal occluder: a single centre study in 236 consecutive patients. Heart. 2003;89: 199–204.
90. Veldtman GR, Razack V, Siu S, El-Hajj H, Walker F, Webb GD, Benson LN, McLaughlin PR. Right ventricular form and function after percutaneous atrial septal defect device closure. J Am Coll Cardiol. 2001;37:2108–13.
91. Rickers C, Jerosch-Herold M, Hu X, et al. Magnetic resonance image-guided transcatheter closure of atrial septal defects. Circulation. 2003;107(1):132–8.
92. Lee T, Tsai IC, Fu YC, Jan SL, Wang CC, Chang Y, Chen MC. MDCT evaluation after closure of atrial septal defect with an Amplatzer septal occluder. AJR Am J Roentgenol. 2007;188(5):W431–9.
93. Murphy JG, Gersh BJ, McGoon MD, et al. Long-term outcome after surgical repair of isolated atrial septal defect: follow-up at 27 to 32 years. N Engl J Med. 1990;323:1645–50.
94. Somerville J, Williams RG, Webb GD. Task force 1: the changing profile of congenital heart disease in adult life. J Am Coll Cardiol. 2001;37:1170–5.
95. Hoffman JI, Kaplan S, Liberthson RR. Prevalence of congenital heart disease. Am Heart J. 2004;147:425–39.
96. Warnes CA, Williams RG, Bashore TM. ACC/AHA 2008 guidelines for the management of adults with congenital heart disease: a report of the American College of Cardiology/American Heart Association Task Force on Practice Guidelines (writing committee to develop guidelines on the management of adults with congenital heart disease). Developed in collaboration with the American Society of Echocardiography, Heart Rhythm Society, International Society for Adult Congenital Heart Disease, Society for Cardiovascular Angiography and Interventions, and Society of Thoracic Surgeons. J Am Coll Cardiol. 2008;52(23): e143–263.

97. Anderson RH, Ho HY, Becker AE. Anatomy of the human atrioventricular junctions revisited. Anat Rec. 2000;260:81–91.
98. Saremi F, Krishnan S. Cardiac conduction system: anatomic landmarks relevant to interventional electrophysiologic techniques demonstrated with 64-detector CT. Radiographics. 2007;27(6):1539–65.
99. Tandon R, Edwards JE. Aneurysm like formations in relation to membranous ventricular septum. Circulation. 1973;47:1089–97.
100. Langer C, Horstkotte D, Piper C. Aneurysm of the membranous septum causes pre-syncopes and transient bilateral blindness. Eur Heart J. 2007;28(7):784.
101. Cheema OM, Patel AA, Chang SM, Shah DJ. Gerbode ventricular septal defect diagnosed at cardiac MR imaging: case report. Radiology. 2009;252(1):50–2.
102. Panduranga P, Mukhaini M. A rare type of Gerbode defect. Echocardiography. 2011;28(6):E118–20.
103. Becu LM, Fontana RS, DuShane JW, Kirklin JW, Burchell HB, Edwards JE. Anatomic and pathologic studies in ventricular septal defects. Circulation. 1956;14:349–64.
104. Moulaert AJ. Anatomy of ventricular septal defect. In: Anderson RH, Shineboume EA, editors. Paediatric cardiology 1977. Edinburgh/London: Churchill Livingstone; 1978. p. 113–24.
105. Soto B, Becker AE, Moulaert AJ, Lie JT, Anderson RH. Classification of ventricular septal defects. Br Heart J. 1980;43:332–43.
106. Sutherland GR, Godman MJ, Smallhorn JF, Guiterras P, Anderson RH, Hunter S. Ventricular septal defects: two dimensional echocardiographic and morphological correlations. Br Heart J. 1982;47:316–28.
107. Lue HC, Sung TC, Hou SH, et al. Ventricular septal defect in Chinese with aortic valve prolapse and aortic regurgitation. Heart Vessels. 1986;2(2):111–6.
108. Capelli H, Andrade JL, Somerville J. Classification of the site of ventricular septal defect by 2-dimensional echocardiography. Am J Cardiol. 1983;51(9):1474–80.
109. Baker EJ, Leung MP, Anderson RH, Fischer DR, Zuberbuhler JR. The cross sectional anatomy of ventricular septal defects: a reappraisal. Br Heart J. 1988;59(3):339–51.
110. Macé L, Dervanian P, Le Bret E, et al. “Swiss cheese” septal defects: surgical closure using a single patch with intermediate fixings. Ann Thorac Surg. 1999;67(6):1754–8.
111. Kirklin JK, Castaneda AR, Keane JF, Fellows KE, Norwood WI. Surgical management of multiple ventricular septal defects. J Thorac Cardiovasc Surg. 1980;80:485–93.
112. Griffin ML, Sullivan ID, Anderson RH, Macartney FJ. Doubly committed subarterial ventricular septal defect: new morphological criteria with echocardiographic and angiocardiographic correlation. Br Heart J. 1988;59(4):474–9.
113. Ozkutlu S, Saraçlar M, Alehan D, Yurdakul Y, Firat P, Tokel K. Subpulmonary and subaortic ridges in doubly committed subarterial ventricular septal defect: an echocardiographic study. Eur Heart J. 1996;17(6):935–9.
114. Newfeld EA, Muster AJ, Paul MH, Idriss FS, Riker WL. Discrete subvalvular aortic stenosis in childhood: study of 51 patients. Am J Cardiol. 1976;38:53–61.
115. al-Marsafawy HM, Ho SY, Redington AN, Anderson RH. The relationship of the outlet septum to the aortic outflow tract in hearts with interruption of the aortic arch. J Thorac Cardiovasc Surg. 1995;109(6):1225–36.
116. Niwa K, Perloff JK, Kaplan S, Child JS, Miner PD. Eisenmenger syndrome in adults: ventricular septal defect, truncus arteriosus, univentricular heart. J Am Coll Cardiol. 1999;34:223–32.
117. Neumayer U, Stone S, Somerville J. Small ventricular septal defects in adults. Eur Heart J. 1998;19(10):1573–82.
118. Backer CL, Winters RC, Zales VR, et al. Restrictive ventricular septal defect: how small is too small to close? Ann Thorac Surg. 1993;56:1014–8.
119. Mongeon FP, Burkhart HM, Ammash NM, et al. Indications and outcomes of surgical closure of ventricular septal defect in adults. JACC Cardiovasc Interv. 2010;3(3):290–7.
120. Lun K, Li H, Leung MP, Chau AK, Yung T, Chiu CS, Cheung Y. Analysis of indications for surgical closure of subarterial ventricular septal defect without associated aortic cusp prolapse and aortic regurgitation. Am J Cardiol. 2001;87:1266–70.
121. Fu Y-C, Bass J, Amin Z, et al. Transcatheter closure of perimembranous ventricular septal defects using the new Amplatzer membranous VSD occluder: result of the U.S. phase I trial. J Am Coll Cardiol. 2006;47:319–25.
122. Tomita H, Arakaki Y, Ono Y, Yamada O, Yagihara T, Echigo S. Impact of noncoronary cusp prolapse in addition to right coronary cusp prolapse in patients with a perimembranous ventricular septal defect. Int J Cardiol. 2005;101(2):279–83.
123. Kumar K, Lock JE, Geva T. Apical muscular ventricular septal defects between the left ventricle and the right ventricular infundibulum. Diagnostic and interventional considerations. Circulation. 1997;95(5):1207–13.
124. Cassels DE. The ductus arteriosus. Springfield: Charles C. Thomas; 1973.
125. Lloyd TR, Beekman III RH. Clinically silent patent ductus arteriosus. Am Heart J. 1994;127:1664–5.
126. Cerruto G, Mancuso L. Systemic and pulmonary embolization in a patient with patent ductus arteriosus. Eur J Echocardiogr. 2005;6(5):376–8.
127. Krichenko A, Benson LN, Burrows P, Moes CA, McLaughlin P, Freedon RM. Angiographic classification of the isolated, persistently patent ductus arteriosus and implications for percutaneous catheter occlusion. Am J Cardiol. 1989;63:877–9.
128. Andrade A, Vargas-Barron J, Rijlaarsdam M, Romero-Cardenas A, Keirns C, Espinola N. Utility of transesophageal echocardiography in the examination of adult patients with patent ductus arteriosus. Am Heart J. 1995;130(3 Pt 1):543–6.

129. Li YL, Wong DT, Wei W, Liu J. A new method for detecting the proximal aortic arch and innominate artery by transesophageal echocardiography. Anesthesiology. 2006;105:226–7.
130. Moore JW, George L, Kirkpatrick SE, et al. Percutaneous closure of the small patent ductus arteriosus using occluding spring coils. J Am Coll Cardiol. 1994;23:759–65.
131. Morgan-Jughes GJ, Marshall AJ, Roobottome C. Morphologic assessment of patent ductus arteriosus in adults using retrospectively ECG-gated multidetector CT. Am J Roentgenol. 2003;181:749–54.
132. Celermajer DS, Sholler GF, Hughes CF, Baird DK. Persistent ductus arteriosus in adults: a review of surgical experience with 25 patients. Med J Aust. 1991;155:233–6.
133. Wang JK, Liau CS, Huang JJ, Hsu KL, Lo PH, Hung JS, et al. Transcatheter closure of patent ductus arteriosus using Gianturco coils in adolescents and adults. Catheter Cardiovasc Interv. 2002;55:513–8.
134. Roques F, Hennequin JL, Sanchez B, Ridarch A, Rousseau H. Aortic stent-graft for patent ductus arteriosus in adults: the aortic exclusion technique. Ann Thorac Surg. 2001;71:1708–9.
135. Hayabuchi Y, Mori K, Kagami S. Virtual endoscopy using multidetector-row CT for coil occlusion of patent ductus arteriosus. Catheter Cardiovasc Interv. 2007;70(3):434–9.
136. Thai WE, Harper RW, Seneviratne S. Dynamic volume 320-slice CT in the assessment of patent ductus arteriosus for percutaneous closure. Heart. 2010;96(4):321.
137. Taneja K, Gulati M, Jain M, Saxena A, Das B, Rajani M. Ductal arteriosus aneurysm in the adult: role of computed tomography in diagnosis. Clin Radiol. 1997;52:231–4.